ATLAS NOTE

ATLAS-CONF-2013-030

March 11, 2013

Measurements of the properties of the Higgs-like boson in the $WW^{(*)} \to \ell\nu\ell\nu$ decay channel with the ATLAS detector using 25 fb^{-1} of proton-proton collision data

The ATLAS Collaboration

Abstract

Evidence for the Higgs-like boson in the $H \to WW^{(*)} \to \ell\nu\ell\nu$ channel is presented using the complete 2012 and 2011 data samples collected with the ATLAS detector at the LHC. The samples correspond, respectively, to an integrated luminosity of 20.7 fb^{-1} at a centre-of-mass energy of 8 TeV and 4.6 fb^{-1} at 7 TeV. The analysis focuses on such a boson in the Standard Model with a mass of $m_H = 125$ GeV, where an excess over the expected number of background events is observed. The significance of the excess is 3.8 standard deviations; the expected value is 3.7. The ratio of the observed and expected numbers of events is consistent with unity, $\mu = 1.01 \pm 0.31$. The case where the signal is accompanied by two or more jets is optimised for the vector boson fusion production process, and the significance of the excess is 2.5 standard deviations; the expected value is 1.6. The product of the Higgs boson cross section at 8 TeV and the branching ratio to $WW^{(*)}$ is measured to be 6.0 ± 1.6 pb; the expected value is 4.8 ± 0.7 pb.

ATLAS-CONF-2013-030
13/03/2013

1 Introduction

In the Standard Model (SM) of particle physics, the Englert-Brout-Higgs mechanism of electroweak symmetry breaking gives mass to all massive elementary particles and predicts the Higgs boson [1–3]. In the summer of 2012, the ATLAS and CMS experiments discovered a Higgs-like boson with a mass of approximately $m_H = 126\,\text{GeV}$ [4, 5]. The current experimental focus is on the measurement of its properties: the spin and the couplings to elementary bosons and fermions.

This note presents the evidence of the SM Higgs-like boson in the $H \to WW^{(*)} \to \ell\nu\ell\nu$ channel ($\ell = e, \mu$) using the complete data samples of 2012 and 2011 taken at $\sqrt{s} = 8$ and 7 TeV, respectively, collected with the ATLAS detector at the LHC. The channel provides input to the overall production rate and the couplings to weak bosons. The analysis techniques are based on an earlier study of the $e\nu\mu\nu$ final state with no accompanying jet or one accompanying jet ($N_{\text{jet}} \leq 1$) [6]. For the results presented in this note, many aspects of the analysis were improved and optimised for a signal with a mass of $m_H = 125\,\text{GeV}$. This signal mass is assumed throughout the note, unless stated otherwise.

The analysis expands the scope of the production mode and the decay channels. The former is the vector boson fusion (VBF) production of the signal accompanied by at least two jets ($N_{\text{jet}} \geq 2$) from the quarks emitting the bosons. The latter are the $e\nu e\nu$ and $\mu\nu\mu\nu$ channels.

The note is organised as follows: Section 2 describes the data and the simulated samples. Section 3 presents the analysis method, introducing the background sources and the key variables m_{T} and $m_{\ell\ell}$. Section 4 details the estimation of the backgrounds yields. Section 5 presents the systematic uncertainties. The focus of the note is on the analysis of the 8 TeV data, but the analysis of the 7 TeV data is briefly described in Section 6. Section 7 presents the evidence for the Higgs-like boson and the associated measurements. Section 8 states the conclusions.

2 Data and simulated samples

The data samples used for this analysis were collected using the ATLAS detector, a multi-purpose particle physics experiment with a forward-backward symmetric cylindrical geometry and near 4π coverage in solid angle. The detector is described in detail elsewhere [7].

The data samples were triggered requiring at least a muon or an electron with $p_{\text{T}} > 24\,\text{GeV}$ that are loosely isolated. The lepton trigger efficiencies are measured using Z candidates as a function of p_{T} and pseudorapidity η. The efficiencies for the leptons used in this analysis, selected as described in Section 3, are approximately 70% for muons with $|\eta| < 1.05$, 90% for muons in the range $1.05 < |\eta| < 2.4$, and 90% for the electrons.

In this analysis, the signal contributions considered include the dominant gluon-gluon fusion production process ($gg \to H$, denoted as ggF), the vector-boson fusion production process ($qq' \to qq'H$, denoted as VBF) and the Higgs-strahlung process ($qq' \to WH, ZH$, denoted as VH). The $t\bar{t}H$ production mechanism is negligible due to its smaller cross section. Only the $H \to WW^{(*)} \to \ell\nu\ell\nu$ (with $\ell = e, \mu$) channels are considered, which include the small contributions from leptonic τ decays. The branching fraction for the decay as a function of m_H is calculated using P 4 [8,9] with H used to calculate the total width [10].

The ggF signal cross section is computed up to next-to-next-to-leading order (NNLO) in QCD [11–16] Next-to-leading order (NLO) electroweak (EW) corrections are also applied [17, 18], as well as QCD soft-gluon resummations up to next-to-next-to-leading log (NNLL) [19]. These calculations are detailed in Refs. [20–22], and assume factorisation between the QCD and EW corrections. The VBF signal cross section is computed with approximate NNLO QCD corrections [23] and full NLO

Table 1: Monte Carlo generators used to model the signal and background processes in which all of the W and Z decay channels are included in the corresponding product of the cross section (σ) and branching fraction ($\mathcal{B}$) at $\sqrt{s} = 8$ TeV. Masses are given in units of GeV. Details are given in the text.

Signal	MC generator	$\sigma \cdot \mathcal{B}$ (pb)
ggF	P [30]+P 8 [31]	0.44
VBF	P +P 8	0.035
VH	P 8	0.13

Background	MC generator	$\sigma \cdot \mathcal{B}$ (pb)
$q\bar{q}, gq \to WW$	P +P 6 [32]	5.7
$q\bar{q}, gq \to WW+2j$	Sherpa [33] with no $\mathcal{O}(\alpha_s)$ terms	0.039
$gg \to WW$	GG2WW 3.1.2 [34, 35]+H [36]	0.16
$t\bar{t}$	MC@NLO [37]+H	240
Single top: tW, tb	MC@NLO+H	28
Single top: tqb	AcerMC [38]+P 6	88
Z/γ^*, inclusive	A +H	16000
$Z^{(*)} \to \ell\ell + 2j$	Sherpa processes up to $\mathcal{O}(\alpha_s)$	1.2
$Z^{(*)}Z^{(*)} \to 4\ell$	P +P 8	0.73
$WZ/W\gamma^*, m_{Z/\gamma^*}>7$	P +P 8	0.83
$W\gamma^*, m_{\gamma^*} \leq 7$	MadGraph [39–41]+P 6	11
$W\gamma$	A +H	370

QCD and EW corrections [24–26]. The cross sections of the associated VH production processes are calculated up to NNLO QCD corrections [27, 28] and NLO EW corrections [29].

The Monte Carlo (MC) generators used to model signal and background processes are listed in Table 1. The number quoted for the inclusive Drell-Yan process (DY), Z/γ^*, is for a range of the invariant mass of the two lepton system that excludes the low-mass region, $m_{\ell\ell} < 10$ GeV. Kinematic criteria are also applied in the event generation of $W\gamma$, where $W \to \ell\nu$, and $W\gamma^*$, where $W \to \ell\nu$ and $\gamma^* \to \ell\ell$. For $W\gamma$ events, the photon must have $p_{\mathrm{T}} > 8$ GeV and be separated from the charged lepton by $\Delta R = ((\Delta\eta)^2 + (\Delta\phi)^2)^{1/2} > 0.25$. For $W\gamma^*$, at least two leptons must have $p_{\mathrm{T}} > 5$ GeV and $|\eta| < 3$ for $ee + \mu\mu$, and $|\eta| < 5$ for $\tau\tau$. (The p_{T} denotes the transverse momentum with respect to the beam line.) Additionally, $m_{\ell\ell} > 2m_e$ is required. (This note follows the convention that the invariant mass of the dilepton system is denoted as $m_{\ell\ell}$ for the dilepton system and similarly for composite systems; the masses of elementary particles are denoted as m_e for electron, m_Z for Z boson, etc.) Interference between the $Z^{(*)}$ and the γ^* is included for $WZ^{(*)}$ and $W\gamma^*$, and the boundary between the samples is at $m_{\ell\ell} = 7$ GeV. For $WZ^{(*)}$ a filter requiring at least two charged leptons with $p_{\mathrm{T}} > 5$ GeV and $|\eta| < 2.8$ is also applied. The $Z^{(*)}Z^{(*)} \to 4\ell$ processes are generated with a $m_{\ell\ell} > 4$ GeV selection. Leptonic decays of W or Z are assumed with the exception of the VH processes, which include all W and Z decays. The quoted cross sections include the branching ratios and are summed over lepton flavours except for the top quark production for which the inclusive cross section is quoted.

For most processes, separate programs are used to generate the hard scattering process and to model the parton showering (PS), hadronisation, and the underlying event (UE). P 8 [31] or P 6 [32] are used for the latter three steps for the signal and some of the background processes. When H [36] is used for the hadronisation and PS, the UE is modelled using J [42]. The W+jets, Z/γ^*+jets and $W\gamma$ processes are described using the A +H generator with the MLM matching scheme described in Ref. [43]. In addition, Sherpa [33] is used for both the hard-scattering process and the parton shower modelling for VBF processes with no $\mathcal{O}(\alpha_s)$ terms, such as $qq \to Zqq$ and non-resonant $qq \to W^+W^-qq$.

The cross sections for the $W\gamma$ and $W\gamma^*$ processes are normalised to the MCFM [44] NLO predictions. These normalisation factors (K-factors) are calculated to be 1.15 for $W\gamma$ and 2.01 for $W\gamma^*$. The K-factor for $W\gamma^*$ is calculated for the phase space criteria $0.5 < m_{\ell\ell} < 7$ GeV, $p_{\mathrm{T}}^{\mathrm{lead}} > 25$ GeV,

$p_{\mathrm{T}}^{\mathrm{sublead}} > 15\,\mathrm{GeV}$, and $|\eta_\ell| < 2.5$, where $p_{\mathrm{T}}^{\mathrm{lead}}$ and $p_{\mathrm{T}}^{\mathrm{sublead}}$ refer to the transverse momenta of the leading and subleading leptons, respectively.

The parton distribution function (PDF) set from CT10 [45] is used for the P and MC@NLO samples, and CTEQ6L1 [46] is used for the A , MadGraph, and P 6/P 8 samples. Acceptances and efficiencies are obtained from a full simulation [47] of the ATLAS detector using G 4 [48]. In two exceptional cases ($q\bar{q}$, $gq \to WW$ and single top processes), fast simulation is used to increase MC statistics. The simulation incorporates a model of the event pile-up conditions in the collected data, including both the effects of multiple pp collisions in the same bunch crossing (denoted as in-time pile-up) and in the nearby bunch crossings (denoted as out-of-time pile-up).

3 Event selection

The analysis in Ref. [49] selected $H \to WW^{(*)} \to e\nu\mu\nu$ candidates with either no accompanying jet or one accompanying jet ($N_{\mathrm{jet}} \leq 1$). In the present analysis, the selection of these candidates is unchanged. Additional decay channels are added by including the $e\nu e\nu$ and $\mu\nu\mu\nu$ final states, and sensitivity to the VBF production mode is obtained by adding candidates with $N_{\mathrm{jet}} \geq 2$. Finally, overall sensitivity is gained by nearly a two-fold increase in statistics.

Basic data quality criteria are applied and a primary vertex is selected as described in Ref. [49]. Two leptons with opposite charge are required; the leading lepton is required to have $p_{\mathrm{T}} > 25\,\mathrm{GeV}$ and the subleading lepton is required to have $p_{\mathrm{T}} > 15\,\mathrm{GeV}$. For the $e\mu + \mu e$ channel, contributions from low-mass $\gamma^* \to \tau\tau \to e\nu\mu\nu$ are rejected with $m_{\ell\ell} > 10\,\mathrm{GeV}$. Similiarly, for the $ee + \mu\mu$ channel low-mass $\gamma^* \to \ell\ell$ is rejected with $m_{\ell\ell} > 12\,\mathrm{GeV}$ and $Z \to \ell\ell$ with $|m_{\ell\ell} - m_Z| > 15\,\mathrm{GeV}$. (This note uses the notation $e\mu + \mu e$ and $ee + \mu\mu$ for the decay channels, where the first symbol denotes the lepton with a higher p_{T}.) The requirements above will be referred to as the "pre-selection" in the rest of this note.

3.1 Leptons

Electron candidates are selected by applying a set of tight identification criteria using a combination of tracking and calorimetric information. The fine lateral and longitudinal segmentation of the calorimeter and the transition radiation detection capability of the ATLAS detector have allowed the previous levels of electron performance [50] to be retained in the increased pile-up environment of the 8 TeV data. The electrons are required to be in the range of $|\eta| < 2.47$ excluding $1.37 < |\eta| < 1.52$, which contains the transition region between barrel and endcap calorimeters. Muon candidates are identified by matching tracks reconstructed in the inner detector and in the muon spectrometer [51]. The muons are required to be in the range $|\eta| < 2.5$. At least one of the lepton candidates must match a trigger object.

Track-based and calorimeter-based isolation criteria [49] are applied to both lepton candidates to further suppress backgrounds from W+ jets and multi-jet production.

3.2 Jets

Jets are reconstructed using the anti-k_t algorithm with distance parameter $R = 0.4$ [52]. The jet energy dependence on in-time pile-up is mitigated by applying two data-derived corrections: one based on the product of the event p_{T} density and the jet area [53], and another that depends on the number of reconstructed primary vertices and the mean number of expected interactions, which primarily affects jets in the forward region. The second correction also addresses the effects of out-of-time pile-up. After the two corrections, energy- and η-dependant MC calibration (typically 40% and ranging from

15% to 100% depending on the η) is applied to all jets. Finally, a residual correction from *in situ* measurements (typically a few percent) is applied to refine the jet calibration [54].

The jets are required to have $p_{\mathrm{T}} > 25\,\mathrm{GeV}$ if $|\eta| < 2.4$ and $p_{\mathrm{T}} > 30\,\mathrm{GeV}$ for $2.4 < |\eta| < 4.5$. The increased threshold in the forward region reduces the contribution from fake jets produced by pile-up. For the $N_{\mathrm{jet}} \geq 2$ analysis, jets with $p_{\mathrm{T}} > 20\,\mathrm{GeV}$ satisfying the JVF requirement, described below, are used in the event selection. Details are discussed later in Section 3.4.

The jet vertex fraction (JVF) is used to reduce the contribution of fake jets from pile-up. It is a ratio computed using charged-particle tracks matched to the jet: the ratio is the sum of the p_{T} of tracks matched to the jet that originate from the primary vertex divided by the sum p_{T} of all tracks matched to the jet. The requirement is $|\,\mathrm{JVF}\,| > 0.5$ for jets with $p_{\mathrm{T}} < 50\,\mathrm{GeV}$. Since it relies on tracking information, JVF is only applied to jets with $|\eta| < 2.4$. The JVF performance is shown in Ref. [49].

The number of jets identified by a b-tagging algorithm ($N_{b\text{-jet}}$) are used for the $N_{\mathrm{jet}} = 1$ and ≥ 2 analyses. These are discussed later in Sections 3.4, 4.3, and 5.3.

3.3 Missing transverse momentum and hadronic recoil

Drell-Yan and multi-jet events are suppressed by requiring large missing transverse momentum [55]. The quantity $E_{\mathrm{T}}^{\mathrm{miss}}$ is the magnitude of $\mathbf{E}_{\mathrm{T}}^{\mathrm{miss}}$, the negative vectorial sum p_{T} of the muons, electrons, photons, jets, and clusters of calorimeter cells not associated with these objects. (In this note, $E_{\mathrm{T}}^{\mathrm{miss}}$ refers to its variants depending on context.) Different selection criteria based on $E_{\mathrm{T}}^{\mathrm{miss}}$ are used depending on the decay channel and jet multiplicity. Variants of $E_{\mathrm{T}}^{\mathrm{miss}}$ are used to deal with the varying pile-up conditions and background composition for the decay channel and jet multiplicity.

3.3.1 $E_{\mathrm{T}}^{\mathrm{miss}}$ selection

For candidates in the $N_{\mathrm{jet}} \leq 1$ modes, a requirement is made on $E_{\mathrm{T,rel}}^{\mathrm{miss}}$ [49], a relative quantity that is the product of the magnitude of $\mathbf{E}_{\mathrm{T}}^{\mathrm{miss}}$ and a projection factor s. The s is either $\sin|\,\Delta\phi_{\mathrm{closest}}\,|$, where $\Delta\phi_{\mathrm{closest}}$ is the azimuthal angle between $\mathbf{E}_{\mathrm{T}}^{\mathrm{miss}}$ and the closest high-p_{T} charged lepton or jet in the transverse plane in the same azimuthal hemisphere, or unity if no such object is present in the event. Figure 1a shows the $E_{\mathrm{T,rel}}^{\mathrm{miss}}$ distribution after the pre-selection requirements but without the selection on $E_{\mathrm{T,rel}}^{\mathrm{miss}}$ itself. The $N_{\mathrm{jet}} = 0$ and $= 1$ $e\mu + \mu e$ channels are shown. Due to a large amount of DY background with fake $E_{\mathrm{T}}^{\mathrm{miss}}$ in events with many pile-up interactions, especially for the 8 TeV data, additional variables are used to further reduce the DY background. An alternative measurement of the missing transverse momentum is obtained using inner detector tracks ($p_{\mathrm{T}}^{\mathrm{miss}}$). Impact parameter and track quality requirements are used to select tracks from the primary interaction. The resolution of this track-based quantity is less sensitive to pile-up interactions than the calorimeter-based $E_{\mathrm{T}}^{\mathrm{miss}}$. The quantity $p_{\mathrm{T}}^{\mathrm{miss}}$ is modified to $p_{\mathrm{T,rel}}^{\mathrm{miss}}$ as was done for $E_{\mathrm{T,rel}}^{\mathrm{miss}}$. Figure 1b shows the $p_{\mathrm{T,rel}}^{\mathrm{miss}}$ distribution after the pre-selection and the requirement on $E_{\mathrm{T,rel}}^{\mathrm{miss}}$ (see Table 2). The $N_{\mathrm{jet}} = 0$ and $= 1$ $ee + \mu\mu$ channels are shown.

The $N_{\mathrm{jet}} \geq 2$ analysis uses $E_{\mathrm{T}}^{\mathrm{miss}}$ and $E_{\mathrm{T,STVF}}^{\mathrm{miss}}$. $E_{\mathrm{T,rel}}^{\mathrm{miss}}$ is not used because the large number of jets reduces the signal efficiency for this criterion. For the $ee + \mu\mu$ channels an additional requirement is made on $E_{\mathrm{T,STVF}}^{\mathrm{miss}}$ in which the soft calorimeter deposits unassociated with high-p_{T} objects are scaled by the soft term vertex fraction. This fraction is the ratio of the scalar sum p_{T} of tracks from the primary vertex unmatched to objects to the scalar sum p_{T} of all tracks in the event also unmatched to objects [56]. The combination of the high level of hadronic activity from the extra jets coming from the hard interaction in addition to the high pile-up conditions makes $E_{\mathrm{T,STVF}}^{\mathrm{miss}}$ a better variable than

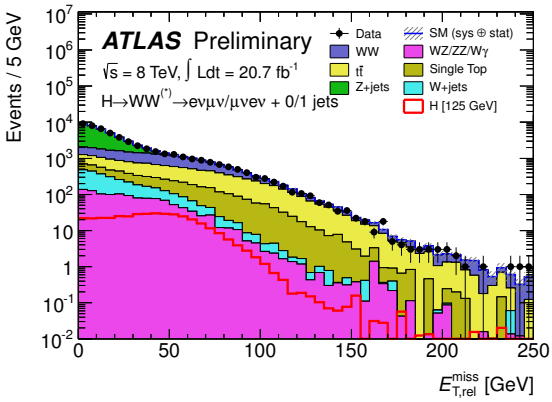

(a) $E_{\mathrm{T,rel}}^{\mathrm{miss}}$ for $N_{\mathrm{jet}} \leq 1$, $e\mu + \mu e$

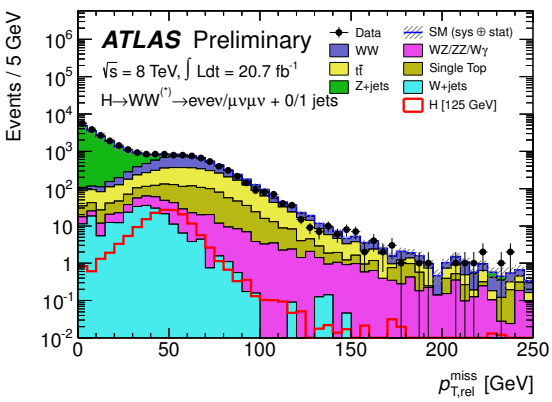

(b) $p_{\mathrm{T,rel}}^{\mathrm{miss}}$ for $N_{\mathrm{jet}} \leq 1$, $ee + \mu\mu$

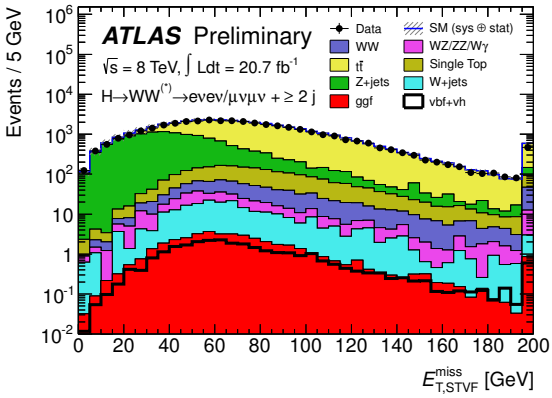

(c) $E_{\mathrm{T,STVF}}^{\mathrm{miss}}$ for $N_{\mathrm{jet}} \geq 2$, $ee + \mu\mu$

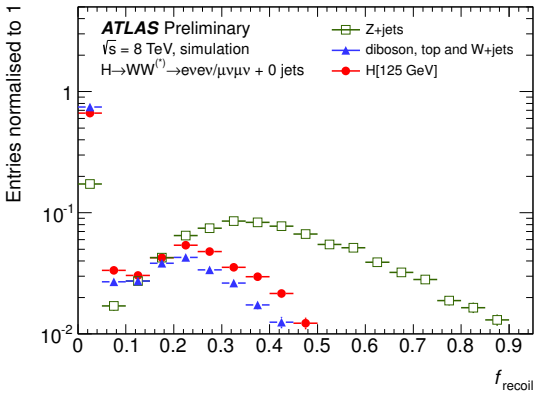

(d) f_{recoil} for $N_{\mathrm{jet}} = 0$, $ee + \mu\mu$

Figure 1: Missing transverse momentum distributions for events after pre-selection for (a) $E_{\mathrm{T,rel}}^{\mathrm{miss}}$ for $N_{\mathrm{jet}} \leq 1$, (b) $p_{\mathrm{T,rel}}^{\mathrm{miss}}$ for $N_{\mathrm{jet}} \leq 1$, and (c) $E_{\mathrm{T,STVF}}^{\mathrm{miss}}$ for $N_{\mathrm{jet}} \geq 2$ modes. The plot in (b) is made after the requirement on $E_{\mathrm{T,rel}}^{\mathrm{miss}}$ and the one in (c) after the requirement on $E_{\mathrm{T}}^{\mathrm{miss}}$. The plot in (d) shows the f_{recoil} distribution in $ee + \mu\mu$ events passing the $N_{\mathrm{jet}} = 0$ selection after $m_{\ell\ell} < 50$ GeV for simulated DY, non-DY and signal processes. The shaded area (too small to be visible in these figures) represents the uncertainty on the signal and background yields from statistical, experimental, and theoretical sources. The signal is overlaid as a red curve in (a) and (b); in (c), the ggF signal is stacked at the bottom while the VBF signal is overlaid as a thick black line. Selections are listed in Table 2. Details are given in Section 3.3.

$p_{\mathrm{T}}^{\mathrm{miss}}$ for this particular case. Figure 1c shows the $E_{\mathrm{T,STVF}}^{\mathrm{miss}}$ distribution after the pre-selection and the requirement on $E_{\mathrm{T}}^{\mathrm{miss}}$ (see Table 2). The $N_{\mathrm{jet}} \geq 2$, $ee + \mu\mu$ channels are shown.

3.3.2 Soft hadronic recoil in Drell-Yan events

The DY background is further reduced by requirements on f_{recoil}, a measurement of the soft hadronic recoil opposite the system of the leptons and any accompanying jet for $N_{\mathrm{jet}} \leq 1$. This quantity is defined for the $N_{\mathrm{jet}} = 0$ mode as the ratio of the recoil momentum and $p_{\mathrm{T}}^{\ell\ell}$, where $\mathbf{p}_{\mathrm{T}}^{\ell\ell} = \mathbf{p}_{\mathrm{T}}^{\ell 1} + \mathbf{p}_{\mathrm{T}}^{\ell 2}$. For the $N_{\mathrm{jet}} = 1$ mode, $p_{\mathrm{T}}^{\ell\ell j}$ is used in place of $p_{\mathrm{T}}^{\ell\ell}$, where $\mathbf{p}_{\mathrm{T}}^{\ell\ell j} = \mathbf{p}_{\mathrm{T}}^{\ell\ell} + \mathbf{p}_{\mathrm{T}}^{j}$. The recoil momentum is the

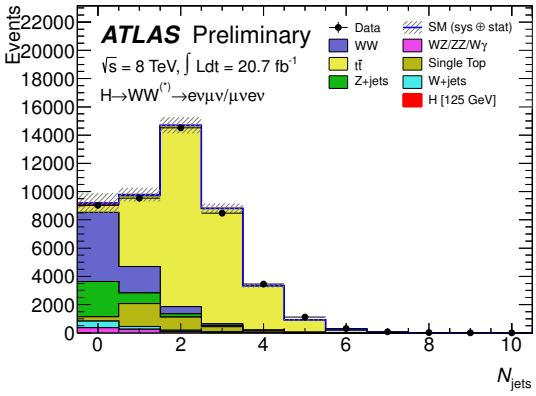

(a) N_{jet} distribution for $e\mu + \mu e$

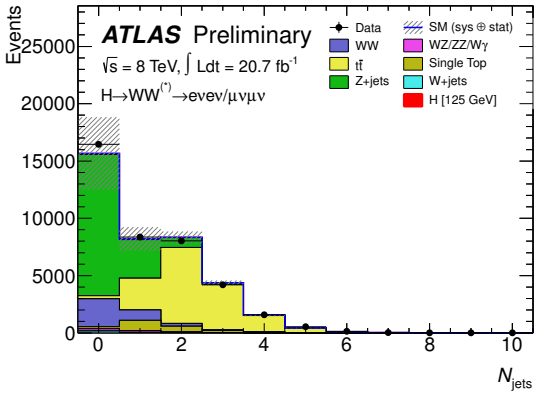

(b) N_{jet} distribution for $ee + \mu\mu$

Figure 2: Jet multiplicity for events in 8 TeV data. The plots are shown for the (a) $e\mu + \mu e$ and (b) $ee + \mu\mu$ channels after pre-selection and $E_{\text{T,rel}}^{\text{miss}} > 25$ GeV and > 45 GeV, respectively. The signal is too small to be seen. The shaded area represents the uncertainty on the signal and background yields from statistical, experimental, and theoretical sources.

vectorial sum p_{T} of the low-p_{T} jets in the ϕ quadrant opposite $\mathbf{p}_{\text{T}}^{\ell\ell}$ for $N_{\text{jet}} = 0$ and $\mathbf{p}_{\text{T}}^{\ell\ell j}$ for $N_{\text{jet}} = 1$. Low-p_{T} jets are defined as those with $p_{\text{T}} > 10$ GeV and below the previously mentioned nominal thresholds. Each low-p_{T} jet is weighted by its JVF value. The f_{recoil} distribution of DY events is distinct from that of non-DY processes, because of the different topology of DY and other events in the dilepton sample. The dilepton system in DY events is balanced by soft hadronic activity, resulting in large values of f_{recoil}, whereas the dilepton system in WW, top, signal, and similar processes is balanced by a combination of recoiling neutrinos and soft hadronic activity, which results in small values of f_{recoil}. Figure 1d shows the f_{recoil} distributions for DY, non-DY and signal processes in simulated events.

3.4 Analyses categorised in N_{jet}

The signal selection strategy depends on the jet multiplicity (N_{jet}) as do the rate and the composition of the backgrounds. For $N_{\text{jet}} \leq 1$ the signal originates almost entirely from the ggF process and WW events dominate the background composition. For $N_{\text{jet}} \geq 2$ the signal is mostly from the VBF process and $t\bar{t}$ events dominate the background. Figures 2a and 2b show the multiplicity distribution of jets in the $e\mu + \mu e$ and $ee + \mu\mu$ channels for all events satisfying pre-selection described and the requirement on $E_{\text{T,rel}}^{\text{miss}}$ (see Table 2). Table 2 summarises the selection described in this section.

For all jet multiplicities, a set of topological selections takes advantage of the configuration of the two leptons. The leptons emerge in the same direction due to the spin correlations of $H \to WW^{(*)}$ decay and the $V - A$ structure of the W decay. The leptons' invariant mass is required to be small, $m_{\ell\ell} < 50$ GeV for $N_{\text{jet}} \leq 1$ and $m_{\ell\ell} < 60$ GeV for $N_{\text{jet}} \geq 2$, and their azimuthal gap is also required to be small, $|\Delta\phi_{\ell\ell}| < 1.8$ radians. The distributions of $m_{\ell\ell}$ and m_{T} are used to extract the signal strength; these variables are introduced later in Section 3.5.

The analysis is divided into $N_{\text{jet}} = 0$, $= 1$, and ≥ 2. In the $N_{\text{jet}} = 0$ analysis, the following criteria improve the rejection of the DY background and multi-jet background. The missing transverse momentum is required to be large. For $e\mu + \mu e$, the selection is $E_{\text{T,rel}}^{\text{miss}} > 25$ GeV. For $ee + \mu\mu$, the selection is tighter, $E_{\text{T,rel}}^{\text{miss}} > 45$ GeV and $p_{\text{T,rel}}^{\text{miss}} > 45$ GeV, because of the large DY background from $Z/\gamma^* \to \ell\ell$.

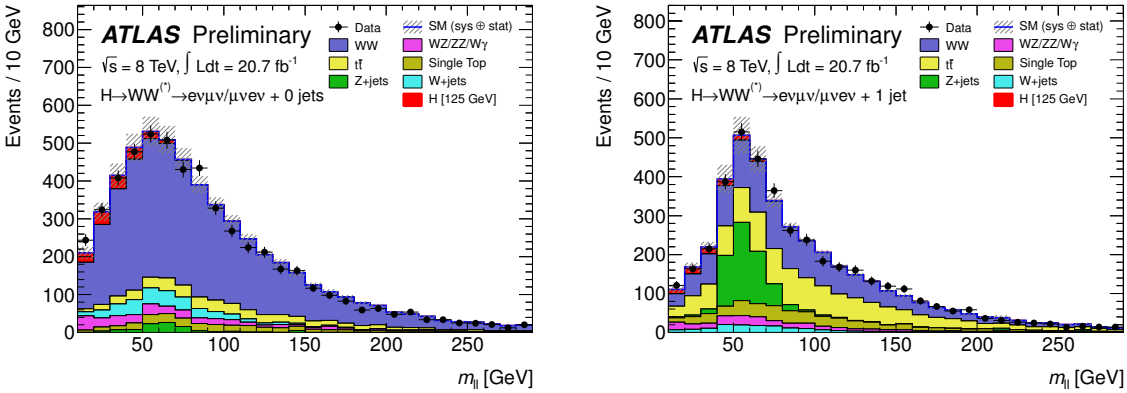

(a) $m_{\ell\ell}$ for $N_{\text{jet}} = 0$, $e\mu + \mu e$

(b) $m_{\ell\ell}$ for $N_{\text{jet}} = 1$, $e\mu + \mu e$

Figure 3: Distribution of $m_{\ell\ell}$ in 8 TeV data. The plots are shown for the $e\mu + \mu e$ channel in (a) $N_{\text{jet}} = 0$ and (b) $N_{\text{jet}} = 1$ modes. The distributions are shown prior to splitting the samples into two $m_{\ell\ell}$ regions for the $e\mu + \mu e$ channel as described in Table 2. The visible signal is stacked on top of the background. The shaded area represents the uncertainty on the signal and background yields from statistical, experimental, and theoretical sources.

The transverse momentum of the dilepton system is required to be large, $p_{\text{T}}^{\ell\ell} > 30\,\text{GeV}$. For $ee + \mu\mu$ events, the hadronic recoil is required to be small, $f_{\text{recoil}} < 0.05$. Finally, the azimuthal gap between $\mathbf{p}_{\text{T}}^{\ell\ell}$ and $\mathbf{E}_{\text{T}}^{\text{miss}}$ (denoted MET in the subscript) is required not to be small in order to remove potentially pathological events, $|\Delta\phi_{\ell\ell,MET}| > \pi/2$.

In the $N_{\text{jet}} = 1$ analysis, the DY treatment is similar to that in $N_{\text{jet}} = 0$ while additional selections further suppress top and $Z/\gamma^* \to \tau\tau$ backgrounds. For DY reduction, the $E_{\text{T,rel}}^{\text{miss}}$ and $p_{\text{T,rel}}^{\text{miss}}$ requirements are the same as in $N_{\text{jet}} = 0$, but the hadronic recoil threshold is higher, $f_{\text{recoil}} < 0.2$. The top background is suppressed by rejecting events with a heavy-flavour jet identified with a multi-variate b-tagging algorithm [57] with 85% efficiency on simulated $t\bar{t}$ events and light-flavour jet mis-tag rate of 11% [58]. The $Z/\gamma^* \to \tau\tau$ background in $e\mu + \mu e$ is suppressed using an invariant mass computed under the assumption that the neutrinos are collinear with the leptons in the τ decay [59] and that they are the only source of $E_{\text{T}}^{\text{miss}}$, $|m_{\tau\tau} - m_Z| \geq 25\,\text{GeV}$.

In the $N_{\text{jet}} \geq 2$ analysis, the event selection follows that in $N_{\text{jet}} = 1$ with the following modifications. The DY is suppressed requiring $E_{\text{T}}^{\text{miss}} > 20\,\text{GeV}$ for $e\mu + \mu e$, and both $E_{\text{T}}^{\text{miss}} > 45\,\text{GeV}$ and $E_{\text{T,STVF}}^{\text{miss}} > 35\,\text{GeV}$ for $ee + \mu\mu$. The VBF-specific selections use the kinematics of the two highest-p_{T} jets in the event (denoted as tag jets). Their rapidity gap is required to be large, $|\Delta y_{jj}| > 2.8$, and their invariant mass is required to be high, $m_{\text{jj}} > 500\,\text{GeV}$. Activity in the rapidity gap between the tag jets is restricted, to reduce the ggF contribution to this mode: events with a jet with $p_{\text{T}} > 20\,\text{GeV}$ inside the rapidity gap are vetoed. The leptons are required to be within the rapidity gap. Finally, $t\bar{t}$ background is further reduced by requiring a small total transverse momentum, $p_{\text{T}}^{\text{tot}} < 45\,\text{GeV}$, where $\mathbf{p}_{\text{T}}^{\text{tot}} = \mathbf{p}_{\text{T}}^{\ell\ell} + \mathbf{p}_{\text{T}}^{jj} + \mathbf{E}_{\text{T}}^{\text{miss}}$, where $\mathbf{p}_{\text{T}}^{jj}$ is the vectorial sum of the transverse momenta of the tag jets.

3.5 Selection summary and signal discriminants $m_{\ell\ell}$ and m_{T}

The signal discriminants $m_{\ell\ell}$ and m_{T}, which appear at the bottom of the table, are introduced to further separate the signal from the background processes. The sample of events at the stage corresponding

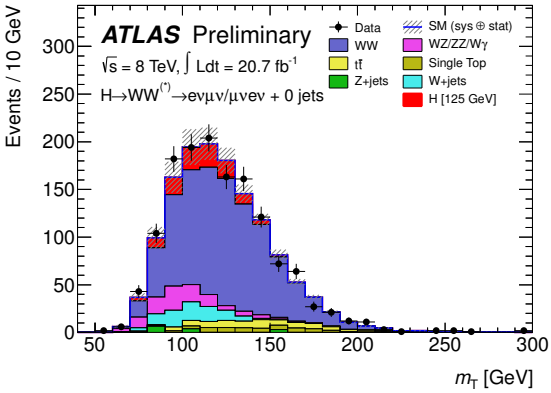

(a) m_{T} for $N_{\mathrm{jet}} = 0$, $e\mu + \mu e$

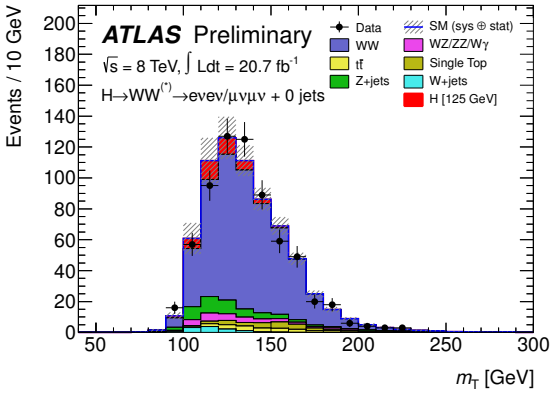

(b) m_{T} for $N_{\mathrm{jet}} = 0$, $ee + \mu\mu$

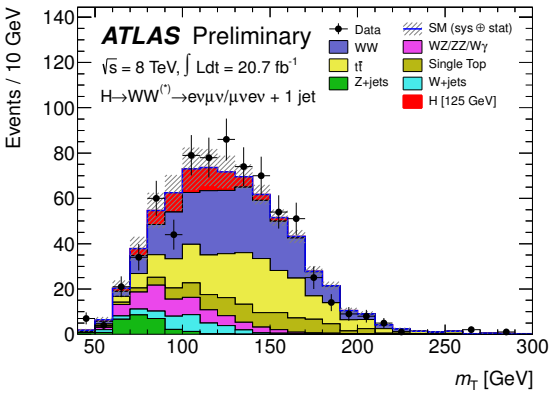

(c) m_{T} for $N_{\mathrm{jet}} = 1$, $e\mu + \mu e$

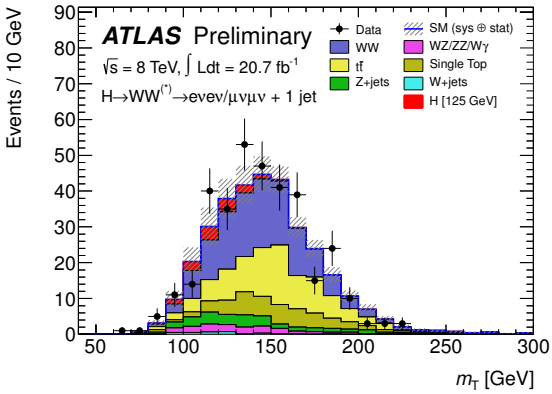

(d) m_{T} for $N_{\mathrm{jet}} = 1$, $ee + \mu\mu$

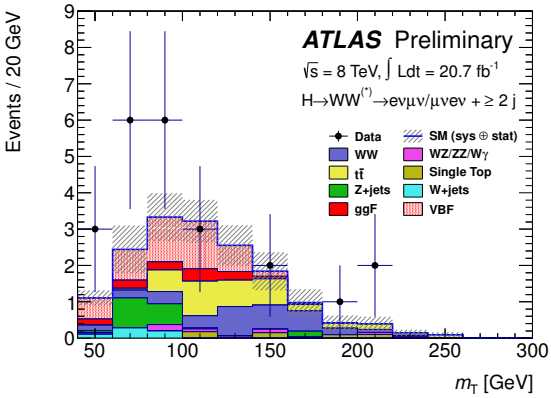

(e) m_{T} for $N_{\mathrm{jet}} \geq 2$, $e\mu + \mu e$

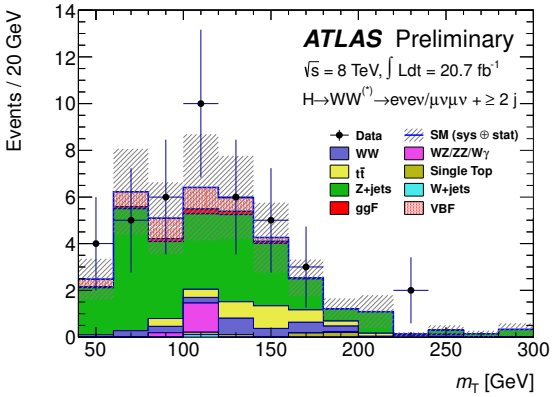

(f) m_{T} for $N_{\mathrm{jet}} \geq 2$, $ee + \mu\mu$

Figure 4: Distribution of the transverse mass, m_{T}, for 8 TeV data. The plots are shown for the $e\mu + \mu e$ (left) and $ee + \mu\mu$ (right) channels in $N_{\mathrm{jet}} = 0$ (top), $N_{\mathrm{jet}} = 1$ (middle), and $N_{\mathrm{jet}} \geq 2$ modes (bottom). The distributions are shown prior to splitting the samples into two $m_{\ell\ell}$ regions for the $e\mu + \mu e$ channel in the $N_{\mathrm{jet}} = 0$ and $= 1$ modes, as described in Table 2. The visible signal is stacked at the top of the background. For the $N_{\mathrm{jet}} \geq 2$ mode, the signal is plotted separately for the ggF and VBF production processes. The shaded area represents the uncertainty on the signal and background yields from statistical, experimental, and theoretical sources.

Table 2: Selection listing for 8 TeV data. The criteria specific to $e\mu + \mu e$ and $ee + \mu\mu$ are noted as such; otherwise, they apply to both. Pre-selection applies to all N_{jet} modes. The rapidity gap is the y range spanned by the two leading jets. The $m_{\ell\ell}$ split is at 30 GeV. The modifications for the 7 TeV analysis are given in Section 6 and are not listed here. Energies, masses, and momenta are in units of GeV.

Category	$N_{\text{jet}} = 0$	$N_{\text{jet}} = 1$	$N_{\text{jet}} \geq 2$
Pre-selection	Two isolated leptons ($\ell = e, \mu$) with opposite charge Leptons with $p_{\text{T}}^{\text{lead}} > 25$ and $p_{\text{T}}^{\text{sublead}} > 15$ $e\mu + \mu e$: $m_{\ell\ell} > 10$ $ee + \mu\mu$: $m_{\ell\ell} > 12$, $\lvert m_{\ell\ell} - m_Z \rvert > 15$		
Missing transverse momentum and hadronic recoil	$e\mu + \mu e$: $E_{\text{T,rel}}^{\text{miss}} > 25$ $ee + \mu\mu$: $E_{\text{T,rel}}^{\text{miss}} > 45$ $ee + \mu\mu$: $p_{\text{T,rel}}^{\text{miss}} > 45$ $ee + \mu\mu$: $f_{\text{recoil}} < 0.05$	$e\mu + \mu e$: $E_{\text{T,rel}}^{\text{miss}} > 25$ $ee + \mu\mu$: $E_{\text{T,rel}}^{\text{miss}} > 45$ $ee + \mu\mu$: $p_{\text{T,rel}}^{\text{miss}} > 45$ $ee + \mu\mu$: $f_{\text{recoil}} < 0.2$	$e\mu + \mu e$: $E_{\text{T}}^{\text{miss}} > 20$ $ee + \mu\mu$: $E_{\text{T}}^{\text{miss}} > 45$ $ee + \mu\mu$: $E_{\text{T,STVF}}^{\text{miss}} > 35$ -
General selection	- $\lvert \Delta\phi_{\ell\ell,MET} \rvert > \pi/2$ $p_{\text{T}}^{\ell\ell} > 30$	$N_{b\text{-jet}} = 0$ - $e\mu + \mu e$: $Z/\gamma^* \to \tau\tau$ veto	$N_{b\text{-jet}} = 0$ $p_{\text{T}}^{\text{tot}} < 45$ $e\mu + \mu e$: $Z/\gamma^* \to \tau\tau$ veto
VBF topology	- - - -	- - - -	$m_{jj} > 500$ $\lvert \Delta y_{jj} \rvert > 2.8$ No jets ($p_{\text{T}} > 20$) in rapidity gap Require both ℓ in rapidity gap
$H \to WW^{(*)} \to \ell\nu\ell\nu$ topology	$m_{\ell\ell} < 50$ $\lvert \Delta\phi_{\ell\ell} \rvert < 1.8$ $e\mu + \mu e$: split $m_{\ell\ell}$ Fit m_{T}	$m_{\ell\ell} < 50$ $\lvert \Delta\phi_{\ell\ell} \rvert < 1.8$ $e\mu + \mu e$: split $m_{\ell\ell}$ Fit m_{T}	$m_{\ell\ell} < 60$ $\lvert \Delta\phi_{\ell\ell} \rvert < 1.8$ - Fit m_{T}

to the selection on the variable of interest is discussed below.

The $m_{\ell\ell}$ distribution for $N_{\text{jet}} \leq 1$ is shown in Fig. 3. The signal-to-background (S/B) ratio in this distribution is varying, so the sample is further subdivided for signal extraction (Section 7.2) at $m_{\ell\ell} = 30$ GeV for $N_{\text{jet}} \leq 1$ in the $e\mu + \mu e$ channels. The split is not made for the corresponding $ee + \mu\mu$ channels.

The transverse mass m_{T} distribution is used to measure the signal strength. It is defined as $m_{\text{T}} = ((E_{\text{T}}^{\ell\ell} + E_{\text{T}}^{\text{miss}})^2 - \lvert \mathbf{p}_{\text{T}}^{\ell\ell} + \mathbf{E}_{\text{T}}^{\text{miss}} \rvert^2)^{1/2}$ with $E_{\text{T}}^{\ell\ell} = (\lvert \mathbf{p}_{\text{T}}^{\ell\ell} \rvert^2 + m_{\ell\ell}^2)^{1/2}$. The statistical treatment is described later in Section 7. Figure 4 shows the expected signal and the composition of the expected background for the different N_{jet} analyses and decay channels. The details of the normalisation of the background events are discussed in the next section. The highest S/B is in a region of m_{T} around m_H: $0.75\, m_H < m_{\text{T}} < m_H$ for $N_{\text{jet}} \leq 1$ and $m_{\text{T}} < 1.2\, m_H$ for $N_{\text{jet}} \geq 2$. To illustrate the relative size of the signal, the expected S/B in the above-mentioned m_{T} range is 0.14, 0.15, and 0.31 for $N_{\text{jet}} = 0$, $= 1$, and ≥ 2, respectively, for the combined $e\mu + \mu e + ee + \mu\mu$ channels.

4 Background estimation

The processes producing two isolated high-p_{T} leptons with high values of $E_{\text{T}}^{\text{miss}}$ are WW and top quark production. In this note, top background refers to the combined $t\bar{t}$ and single top (tW, tb, and tqb) processes unless stated otherwise the latter is noted as t in the tables. These backgrounds, as well as

$Z/\gamma^* \to \tau\tau$ background, are each normalised to the observed rate in a data control region (CR) defined to be as pure as possible for the relevant background source. The processes $Z/\gamma^* \to \ell\ell$ and $Z/\gamma^* \to \tau\tau$ are noted as Z/γ^* in the tables and $Z+$jets in the figure legends. Table 3 summarises the treatment of the backgrounds. An overview of the CR statistics is given in Table 4, and is discussed later in Section 4.5.

The $W+$jets background is estimated from data using corrections derived from simulation, as described in Section 4.1.1. The shapes and normalisation of backgrounds from diboson processes other than WW ($W\gamma^{(*)}$, $WZ^{(*)}$, and $Z^{(*)}Z^{(*)}$) are estimated using simulation; these processes are noted as VV in the tables. The simulation predictions for these backgrounds are cross-checked, together with the $W+$jets data-derived estimation, by requiring that the two lepton candidates have the same charge. This validation region is to be distinguished from the CRs, which are used to normalise the most significant backgrounds.

The DY background is relatively small in this analysis because it is suppressed by the $E_{\mathrm{T}}^{\mathrm{miss}}$, $p_{\mathrm{T}}^{\mathrm{miss}}$, f_{recoil}, and $m_{\ell\ell}$ criteria described in Section 3. As shown in Table 2, the selection on $E_{\mathrm{T}}^{\mathrm{miss}}$ is much tighter for the $ee+\mu\mu$ channel than for the $e\mu+\mu e$ channel because of the larger DY background from $Z/\gamma^* \to \ell\ell$ as compared to $Z/\gamma^* \to \tau\tau \to e\nu\mu\nu$, respectively. For this reason, the use of the Z peak as a CR is subject to large uncertainties from mismodelling of the $E_{\mathrm{T}}^{\mathrm{miss}}$ tails as a function of $m_{\ell\ell}$. Therefore, a data-derived method is used to estimate the DY background for $ee+\mu\mu$, as described in Section 4.1.2 . In the case of $e\mu+\mu e$, where the majority of the background comes from $Z/\gamma^* \to \tau\tau$, a CR is used, and the details are described in Section 4.2. For $N_{\mathrm{jet}} \geq 2$, processes with up to one QCD vertex producing quark jets are non-negligible; they account for approximately 20% of the total DY background for $e\mu+\mu e$ and 6% for $ee+\mu\mu$.

The CRs and validation regions are defined by selections similar to those used for the signal region, but with some criteria reversed or modified to obtain signal-depleted samples enriched in particular backgrounds. The MC WW background in both the $N_{\mathrm{jet}}=0$ and $N_{\mathrm{jet}}=1$ analyses and the MC top background in the $N_{\mathrm{jet}}=1$ and $N_{\mathrm{jet}} \geq 2$ analyses are normalised to the data yields in the corresponding CRs, after subtracting contributions from processes other than the targeted one. The resulting estimated event yield for that process is extrapolated from the CR to the signal region using the ratio of event yields in the simulation. Using this ratio reduces the sensitivity of the background predictions to systematic uncertainties, which are detailed in Section 5. In general, the $e\mu+\mu e$ CRs with higher statistics, and significantly higher purity than the corresponding $ee+\mu\mu$ channels, are used as CRs for the latter. The exception to this is the top $N_{\mathrm{jet}} \geq 2$ CR where the DY contribution is negligible. Details on the normalisation of the top and WW backgrounds are given in Sections 4.3 and 4.4.

The correlations introduced among the backgrounds by the presence of other processes in the CRs are fully incorporated in the statistical procedure used to test the background-only hypothesis and extract the signal strength (see Section 7). In the following, each background estimate is described after any others on which it depends. For this reason, the largest background (WW) is described last.

4.1 Data-derived estimates of $W+$ jets and $Z/\gamma^* \to \ell\ell$

4.1.1 $W+$ jets estimation and the same-charge validation region

The $W+$jets background contribution is estimated using a CR in which one of the two leptons satisfies the identification and isolation criteria described in Section 3, and the other lepton (denoted as anti-identified) fails these criteria but satisfies a loosened selection. The dominant contribution to this background comes from $W+$jets events in which a jet produces an object which is reconstructed as a lepton. The estimation of this background is unchanged from Ref. [49] except that the extrapolation

Table 3: Background treatment listing. The estimation procedures for various background processes are given in four categories: normalised using a control region (CR); data-derived estimate (Data); normalised using the MC (MC); and normalised using the MC, but validated in a control region (MC + VR). The "($e\mu + \mu e$)" terms denote that for the $ee + \mu\mu$ channel in the same N_{jet} mode, the $e\mu + \mu e$ region is used instead, for reasons of purity and/or statistics. The "(merged)" terms indicate that the fully combined $e\mu + \mu e + ee + \mu\mu$ control region is used for all channels.

Channel	WW	Top	$Z/\gamma^* \to \tau\tau$	$Z/\gamma^* \to \ell\ell$	W+ jets	VV
$N_{\text{jet}} = 0$						
$e\mu + \mu e$	CR	CR	CR	MC	Data	MC + VR
$ee + \mu\mu$	CR ($e\mu + \mu e$)	CR ($e\mu + \mu e$)	CR ($e\mu + \mu e$)	Data	Data	MC + VR
$N_{\text{jet}} = 1$						
$e\mu + \mu e$	CR	CR	CR	MC	Data	MC + VR
$ee + \mu\mu$	CR ($e\mu + \mu e$)	CR ($e\mu + \mu e$)	CR ($e\mu + \mu e$)	Data	Data	MC + VR
$N_{\text{jet}} \geq 2$						
$e\mu + \mu e$	MC	CR (merged)	CR	MC	Data	MC
$ee + \mu\mu$	MC	CR (merged)	CR ($e\mu + \mu e$)	Data	Data	MC

to the signal region from the CR is done as a function of the p_{T} and η of the anti-identified lepton. The previous estimation did not distinguish the η values.

The W+ jets background in the signal region is obtained by scaling the number of events in the data CR by a fake factor. The fake factor is defined as the ratio of the number of fully identified lepton candidates passing all selections to the number that are anti-identified. It is estimated as a function of the anti-identified lepton p_{T} and η using an inclusive dijet data sample.

The fake factor uncertainty is the main uncertainty on the W+ jets background estimation. It is dominated by differences in jet composition between dijet and W+ jets samples as observed in MC simulation. The total fake factor uncertainty is 45% (40%) for mis-identified electrons (muons). Unlike the previous treatment [49] of this background, this systematic uncertainty is treated as uncorrelated between electrons and muons. This reduces the effective uncertainty on the total W+ jets background, which yields approximately 30% across different N_{jet} categories.

The processes producing the majority of same-charge dilepton events, namely, W+ jets, $W\gamma^{(*)}$, $WZ^{(*)}$, and $Z^{(*)}Z^{(*)}$, are all backgrounds to $H \to WW^{(*)} \to \ell\nu\ell\nu$. The comparison of the predicted and observed rate and kinematics of these events is used to validate the background predictions. As an example, the m_{T} and $m_{\ell\ell}$ distributions of same-charge $N_{\text{jet}} = 0$ events passing pre-selection and the $|\Delta\phi_{\ell\ell,MET}|$ and $p_{\text{T}}^{\ell\ell}$ requirements are shown in Fig. 5. The total uncertainty on the background prediction shown in these figures includes the systematic uncertainties on the W+ jets background and the other non-WW diboson backgrounds. The uncertainty on the total non-WW diboson background in the signal region is 16% and 22% for $N_{\text{jet}} = 0$ and = 1, respectively.

The $W\gamma$ background arises from the photon converting into an electron-positron pair, while the W decay provides the second muon or electron and the $E_{\text{T}}^{\text{miss}}$ signatures. The simulation of the $W\gamma$ background is checked in a modified same-charge validation region in which the electron selection criteria that remove photon conversions are reversed. In this region, a high $W\gamma$ purity of approximately 80% is obtained. In the complete 8 TeV data sample, the numbers of observed events are 323 and 365 for the $N_{\text{jet}} = 0$ and $= 1$ $W\gamma$ validation regions, which is to be compared to the expected values of 331 ± 12 (stat.) and 380 ± 16 (stat.) events, respectively.

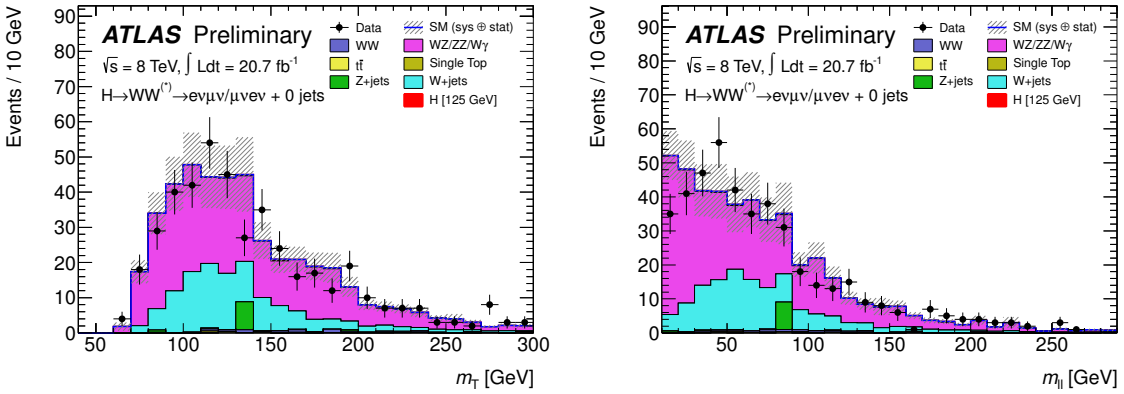

(a) m_{T} for same-charge

(b) $m_{\ell\ell}$ for same-charge

Figure 5: Distribution of (a) m_{T} and (b) $m_{\ell\ell}$ in the same-charge validation region in $N_{\mathrm{jet}} = 0$ after the $p_{\mathrm{T}}^{\ell\ell}$ selection. The shaded area represents the uncertainty on the signal and background yields from statistical, experimental, and theoretical sources. Table 2 lists the selection order.

4.1.2 $Z/\gamma^* \to \ell\ell$

The $Z/\gamma^* \to \ell\ell$ yield in the $ee + \mu\mu$ channel is estimated using a data-derived method. For the $N_{\mathrm{jet}} \leq 1$ modes, the distribution of the hadronic recoil variable f_{recoil} (Section 3.3.2) is used to reduce and estimate the DY, where the reduction is critical due to its relative magnitude. For the $N_{\mathrm{jet}} \geq 2$ mode, the distribution of $E_{\mathrm{T}}^{\mathrm{miss}}$-$m_{\ell\ell}$ is used to estimate DY. The lack of statistics as well as the added difficulty due to the higher jet multiplicity make it more difficult to implement the f_{recoil} method.

For the $N_{\mathrm{jet}} \leq 1$ modes, the efficiencies of the f_{recoil} selection for DY and non-DY processes are measured in data: the DY-dominated $ee + \mu\mu$ in the Z peak region and the non-DY-dominated $e\mu + \mu e$ in the region after the signal selections, respectively. Since the observed fraction of events passing the f_{recoil} selection in the $ee + \mu\mu$ signal region corresponds to the weighted average of the efficiencies, the term corresponding to the DY component is the estimate of the relative fraction of the DY contamination.

Systematic uncertainties are assessed for each assumption. The difference in the non-DY f_{recoil} efficiency between $e\mu + \mu e$ and $ee + \mu\mu$ channels is checked in simulation and validated in data by using the low-p_{T} objects in the recoil calculation, but computed in the region perpendicular to the $\mathbf{p}_{\mathrm{T}}^{\ell\ell}$ and $\mathbf{p}_{\mathrm{T}}^{\ell\ell j}$ direction for $N_{\mathrm{jet}} = 0$ and $= 1$, respectively. The difference in the DY f_{recoil} efficiency between the Z peak and the low $m_{\ell\ell}$ regions in the $ee + \mu\mu$ channel is checked in simulation and validated in data in the $E_{\mathrm{T,rel}}^{\mathrm{miss}} < 30\,\mathrm{GeV}$ region. The differences summed in quadrature are taken as a systematic uncertainty on the extrapolated efficiency. The largest contribution is the 27% assigned for the DY extrapolation from the Z peak region to the low-$m_{\ell\ell}$ region. The total uncertainty on this background is 60% and 80% in the $N_{\mathrm{jet}} = 0$ and $= 1$ modes, respectively.

The $N_{\mathrm{jet}} \geq 2$ uses the $E_{\mathrm{T}}^{\mathrm{miss}}$-$m_{\ell\ell}$ distribution using the events in the Z peak to extrapolate a near-by region ($m_{\ell\ell} < 50\,\mathrm{GeV}$, low $E_{\mathrm{T}}^{\mathrm{miss}}$) to the signal region ($m_{\ell\ell} < 50\,\mathrm{GeV}$, high $E_{\mathrm{T}}^{\mathrm{miss}}$). A small correlation of $(3 \pm 10\,(\mathrm{stat.}))\%$ is found in simulation and the correction is applied. The modeling of the VBF selections is evaluated separately using events with low values of $E_{\mathrm{T}}^{\mathrm{miss}}$ rich in $Z/\gamma^* \to \ell\ell$. The total uncertainty on the background is 15%, which is dominated by experimental sources.

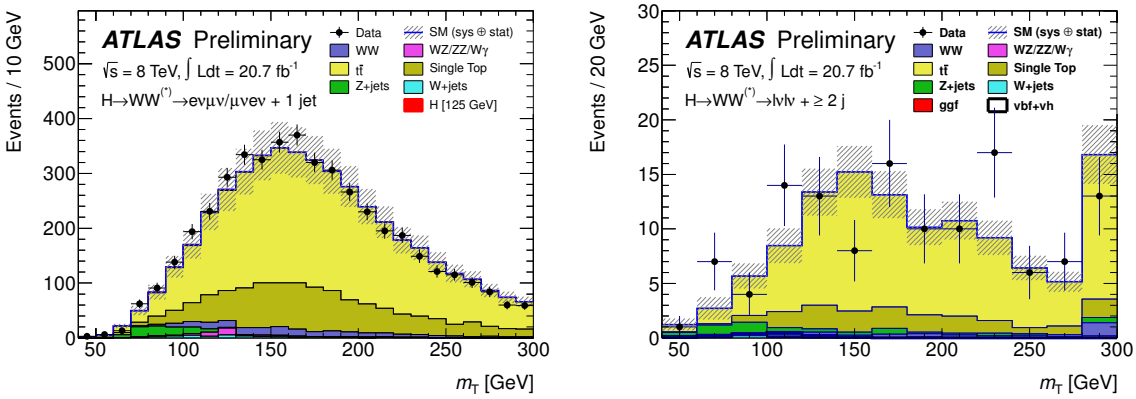

(a) $N_{\text{jet}} = 1$ (b) $N_{\text{jet}} \geq 2$

Figure 6: Distributions of m_{T} in (a) $N_{\text{jet}} = 1$ and (b) $N_{\text{jet}} \geq 2$ top background control regions. The distributions are normalised to the data. The right-most bin in (b) represents the overflow. The shaded area represents the uncertainty on the signal and background yields from statistical, experimental, and theoretical sources.

4.2 $Z/\gamma^* \to \tau\tau$ control region

The DY background from taus is normalised to the data using a $e\mu + \mu e$ CR that is defined by the back-to-back configuration of the leptons, $|\Delta\phi_{\ell\ell}| > 2.8$, and the procedure is unchanged from Ref. [49]. The CR has a purity of 94% and 74% for $N_{\text{jet}} = 0$ and $= 1$, respectively. The total relative uncertainty on the background is 15% and 40% for $N_{\text{jet}} = 0$ and $= 1$, respectively.

The $N_{\text{jet}} \geq 2$ analysis follows the above prescription, but requiring $N_{b\text{-jet}} = 0$ and $p_{\text{T}}^{\text{tot}} < 45$ GeV to define a CR with 67% purity. This sample is used to correct the modelling of $E_{\text{T}}^{\text{miss}}$ while a separate CR in the $Z/\gamma^* \to \ell\ell$ peak region is used to correct the modelling of the VBF-related criteria. The total relative uncertainty on this background is 32%.

4.3 Top control region

The top background for the $N_{\text{jet}} = 0$ mode is estimated using the procedure described in Ref. [49]. The number of top events with no jets is estimated from the number of events in data passing the $E_{\text{T,rel}}^{\text{miss}}$ requirement but having any number of reconstructed jets, a sample that is dominated by top, multiplied by the fraction of top events with no reconstructed jets in simulation. The estimate is corrected using a b-tagged CR. The MC normalisation factor of 1.07 ± 0.03 (stat.) is found. The total uncertainty on this background is 13%.

The top background in the $N_{\text{jet}} = 1$ and ≥ 2 channels is normalised to the data in a CR defined by $N_{b\text{-jet}} = 1$ with the requirements on $|\Delta\phi_{\ell\ell}|$ and $m_{\ell\ell}$ removed. The resulting normalisation factor is 1.04 ± 0.02 (stat.) and 0.59 ± 0.07 (stat.) in the $N_{\text{jet}} = 1$ and ≥ 2 channels, respectively. The latter value reflects the limitation of the non-VBF simulation in the corner of phase space with $m_{jj} > 500$ GeV and $|\Delta y_{jj}| > 2.8$. The total uncertainty for this background is 28% and 39% in the $N_{\text{jet}} = 1$ and ≥ 2 channels, respectively. The observed and expected m_{T} distributions for events in the top CRs are shown in Fig. 6, after applying the appropriate normalisation factors for various background processes.

4.4 WW estimation

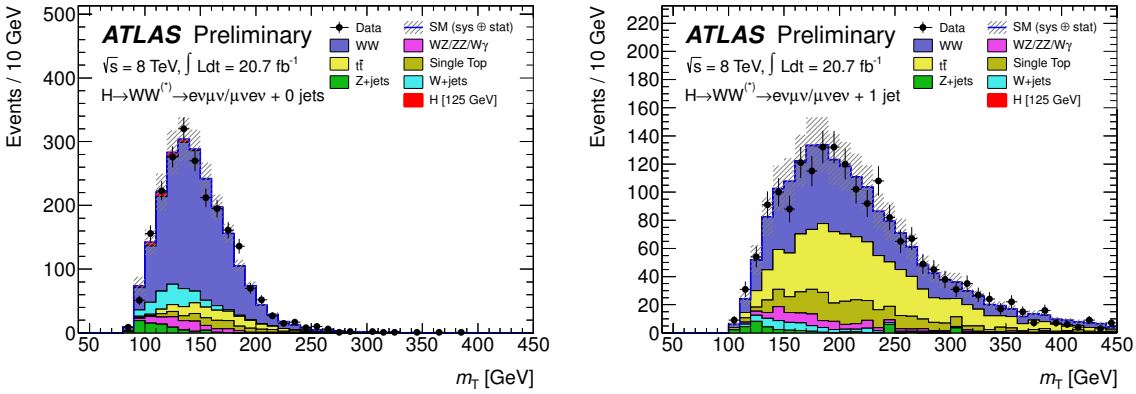

(a) m_{T} for $N_{\mathrm{jet}} = 0$

(b) m_{T} for $N_{\mathrm{jet}} = 1$

Figure 7: Distributions of m_{T} in the WW control region in the (a) $N_{\mathrm{jet}} = 0$ and (b) $N_{\mathrm{jet}} = 1$ modes. The distributions are normalized to the data. The top and $Z/\gamma^* \to \tau\tau$ backgrounds are scaled using the normalisation derived from the corresponding control regions described in the text. The shaded area represents the uncertainty on the signal and background yields from statistical, experimental, and theoretical sources.

The WW background is the dominant background in $N_{\mathrm{jet}} = 0$, comparable to the top background in $N_{\mathrm{jet}} = 1$, and subleading but still significant in the $N_{\mathrm{jet}} \geq 2$ channel. The predictions in the $N_{\mathrm{jet}} = 0$ and $= 1$ analyses are normalised using control regions. The $N_{\mathrm{jet}} \geq 2$ prediction is taken from simulation because of the difficulty of isolating a kinematic region that is sufficiently free of top background background while still retaining high statistics.

The WW CRs for $N_{\mathrm{jet}} \leq 1$ are defined with the same selection as the signal region except that the $|\Delta\phi_{\ell\ell}|$ requirement is removed and the $m_{\ell\ell}$ bound is modified. For $N_{\mathrm{jet}} = 0$, $50 \leq m_{\ell\ell} < 100$ GeV defines the CR; this is a modification with respect to Ref. [6]. The smaller extrapolation in phase space results in a reduction of the systematic uncertainty. For $N_{\mathrm{jet}} = 1$, $m_{\ell\ell} > 80$ GeV defines the CR as was done in Ref. [6].

Events from WW contribute about 70% and 40% of the total events in the $N_{\mathrm{jet}} = 0$ and $= 1$ CRs, respectively. Contributions from sources other than WW are derived as they are for the signal region, including the top and W+jets backgrounds. The resulting WW normalisation factors are 1.16 ± 0.04 (stat.) and 1.03 ± 0.06 (stat.) for the $N_{\mathrm{jet}} = 0$ and $= 1$ signal regions, respectively. The observed and predicted m_{T} distributions for events in the WW CRs are shown in Fig. 7, after applying the appropriate normalisation factors for various background processes.

The total uncertainty on the background is 7.4%, 37%, and 37% for the $N_{\mathrm{jet}} = 0$, $= 1$, and ≥ 2 modes, respectively. The WW and top background estimates for $N_{\mathrm{jet}} = 1$ are anti-correlated due to the large contamination of top quark events in the WW control region. Finally, contributions from multiple parton interactions have been found to be negligible.

4.5 Summary of background estimates

Table 4 shows the expected and observed number of events in the CRs described above, which are used to normalise the Monte Carlo prediction using the data yields. These include the WW in the $N_{\mathrm{jet}} = 0$ and $= 1$ analyses, $Z/\gamma^* \to \tau\tau$ in the $N_{\mathrm{jet}} = 0$, $= 1$, and ≥ 2 analyses and top background in the $N_{\mathrm{jet}} = 1$ and ≥ 2 analyses.

Table 4: Control region yields for 8 TeV data. The observed (N_{obs}) and expected (N_{exp}) yields for the signal (N_{sig}) and background (N_{bkg}) processes are given. The composition of N_{bkg} is given on the right. For $N_{\text{jet}} \geq 2$, $N_{\text{sig,ggF}}$ is added to N_{bkg}. In general, no normalisation factors are applied with the following exception: the top and $Z/\gamma^* \to \tau\tau$ normalisation factors are applied for the corresponding estimates in the WW CRs. All uncertainties are statistical.

Estimate	N_{obs}	N_{bkg}	N_{sig}	N_{WW}	N_{VV}	$N_{t\bar{t}}$	N_t	N_{Z/γ^*}	$N_{W+\text{jets}}$
WW									
$N_{\text{jet}} = 0$	2224	1970 ± 17	31 ± 0.7	1383 ± 9.3	100 ± 6.8	152 ± 4.4	107 ± 4.3	68 ± 10	160 ± 3.6
$N_{\text{jet}} = 1$	1897	1893 ± 17	1.9 ± 0.3	752 ± 6.8	88 ± 5.5	717 ± 9.5	243 ± 6.7	37 ± 7.5	56 ± 2.5
$Z/\gamma^* \to \tau\tau$									
$N_{\text{jet}} = 0$	1935	2251 ± 31	2.5 ± 0.2	61 ± 1.9	8.5 ± 1.1	4.5 ± 0.8	2.7 ± 0.6	2113 ± 31	61 ± 3.8
$N_{\text{jet}} = 1$	2884	3226 ± 34	7.5 ± 0.3	117 ± 2.7	22 ± 3.1	570 ± 8.4	50 ± 3	2379 ± 32	88 ± 4.3
$N_{\text{jet}} \geq 2$	212	224 ± 7	0.6 ± 0.1	13 ± 1	4 ± 1	44 ± 3	5 ± 1	148 ± 6	9 ± 1
Top									
$N_{\text{jet}} = 1$	4926	4781 ± 26	12 ± 0.5	184 ± 3.7	43 ± 9.5	3399 ± 20	1049 ± 13	72 ± 3.1	35 ± 2.2
$N_{\text{jet}} \geq 2$	126	201 ± 5	1.6 ± 0.1	6.4 ± 0.4	1.0 ± 0.3	157 ± 4	26 ± 2	9 ± 1	0.3 ± 0.4

The distributions in the CRs show satisfactory agreement between the data and the MC given the systematic uncertainties on the latter, which are dominated by the overall theoretical uncertainties on the various background contributions. These uncertainties do not propagate to the signal regions because they are replaced by the statistical uncertainties on the data. The extrapolation uncertainties are discussed in more detail in the next section.

5 Systematic uncertainties

The systematic uncertainties on the signal yields and cross section can be divided into two categories: experimental uncertainties such as those on the jet energy scale and the b-jet tagging efficiency, and theoretical uncertainties such as the estimation of the effect of higher-order terms through variations of the QCD scale inputs to Monte Carlo calculations. Some of these uncertainties are correlated between the signal and background predictions, so the impact of each uncertainty is calculated by varying the parameter in question and coherently recalculating the signal and background event yields. For the largest backgrounds normalised using control regions (WW for $N_{\text{jet}} \leq 1$ and top in $N_{\text{jet}} = 1$ and ≥ 2), the theoretical and experimental uncertainties on the extrapolation are described below and the total uncertainties on these backgrounds, as quoted in Section 4, are summarised at the end of this section.

5.1 Theoretical uncertainties on the Higgs signal

Theoretical uncertainties on the signal production cross sections include uncertainties on the QCD renormalisation and factorisation scales, on the PDF model used to evaluate the cross section and acceptance, and on the underlying event and parton shower model used in the signal model [60, 61]. To evaluate the uncertainties from the QCD factorisation and renormalisation scales, the scales are independently varied up and down by a factor of two while keeping their ratio between 0.5 and 2.

For the ggF signal contribution in the $N_{\text{jet}} = 0$ and $= 1$ analyses, the QCD scale uncertainties on the inclusive cross sections for events with $N_{\text{jet}} \geq 0$, ≥ 1, and ≥ 2 are assumed to be independent [62]. Those uncertainties are approximately 8%, 20%, and 70%, respectively, and are calculated using the inclusive ggF process from the HHNLO program [63,64]. They are converted into uncertainties on the

cross sections in exclusive jet multiplicity final states according to the prescription in Refs. [61,62,65]. The uncertainties on the inclusive cross sections are shared across the exclusive jet multiplicity categories, and in practice introduce anti-correlations among the predicted signal yield for the different final states representing the migration of events among different jet multiplicities. The sum in quadrature of those uncertainties are 17% and 37% for $N_{\text{jet}} = 0$ and $= 1$, respectively.

Scale uncertainties on the ggF process as it appears in $N_{\text{jet}} \geq 2$ are evaluted using the same procedure. In this case, two inclusive ggF processes are considered: events with at least two jets and passing VBF-specific jet cuts but ignoring the central jet veto, and events with at least three jets, at least one of which would cause the event to fail the central jet veto. MCFM [66] is used to evaluate the cross sections under varied renormalisation and factorisation scales. A relative scale uncertainty of 43% is assigned on the cross section for ggF events passing the VBF selection results.

The total scale uncertainty on the signal combines the ggF and VBF contributions. For the VBF signal, the QCD scale uncertainty on the inclusive cross section is estimated to be less than a percent and therefore is negligible. The large scale uncertainties on the ggF mode are correspondingly diluted in the uncertainty on the total signal yield, particularly for higher jet multiplicities. The corresponding uncertainties on the total signal yield are 17%, 30%, and 7% for the $N_{\text{jet}} = 0$, $= 1$, and ≥ 2 analyses, respectively. The total QCD scale uncertainty on the signal includes an additional contribution of about 4%, corresponding to the QCD scale uncertainty on the acceptance alone, which is correlated among the jet multiplicities.

The PDF uncertainties on the signal cross section and acceptance are evaluated following Refs. [45, 67–69], using the envelopes of error sets as well as different PDF sets, applied separately to quark-quark, quark-gluon, and gluon-gluon initiated processes. The dependence on the value of $\alpha_s(M_Z)$ used is also included. The relative PDF uncertainty is 8% for the ggF and $t\bar{t}H$ process and $3-4\%$ for the quark-initiated VBF and VH processes. These uncertainties are estimated by following the prescription in Ref. [67] and by using the PDF sets of CT10 [45], MSTW [68], and NNPDF [69]. The PDF uncertainties are assumed to be completely correlated among processes with identical initial states, regardless of whether or not they are signal or background processes.

Uncertainties on the P +P 8 modelling of signal processes, particularly the sensitivity to the underlying event and parton shower model, are estimated by comparison to MC@NLO+H . The resulting uncertainties are 3% for the $N_{\text{jet}} = 0$ signal and 10% for the $N_{\text{jet}} = 1$ signal, anti-correlated between the jet multiplicity bins. For the $N_{\text{jet}} \geq 2$ analysis, the uncertainty on the effect of UE modelling is evaluated through comparison of P +P 6 samples generated with and without the UE, and is 9% for the ggF process and 3% for the VBF process.

5.2 Theoretical uncertainties on background normalisations

For backgrounds such as WW and top that are evaluated through extrapolation from a signal-depleted CR, theoretical uncertainties are reduced compared to those on the absolute MC normalisation. The extrapolation to the signal region must still be derived from simulation, so some theoretical uncertainties remain. The parameters are defined generally as the ratio of the number of events passing the signal region selection to the number passing the CR selection as evaluated in simulation, $\alpha = N_{\text{SR}}/N_{\text{CR}}$. These are discussed in more detail below. For small backgrounds, such as $W\gamma^{(*)}$ and WZ, the background acceptance is completely evaluated from simulation and calculated cross sections are used for their normalisation, and as a result, the associated theoretical uncertainties are larger than those for backgrounds normalised in CRs. The treatment of these backgrounds is unchanged from Ref. [49].

For WW, the parameters α_{WW}^{0j} and α_{WW}^{1j} denote the extrapolation parameters for $N_{\text{jet}} = 0$ and $= 1$, respectively. The uncertainties on these parameters are evaluated according to the prescription of

Table 5: Uncertainties on the extrapolation parameters α for the WW background in the $N_{\text{jet}} = 0$ and $= 1$ channels. Uncertainties due to the QCD scale, PDF, parton shower (PS), underlying event (UE), and modelling of the NLO qq, $gq \to WW$ processes are given. Each source, represented by a column, is assumed to be uncorrelated, but for a given source the uncertainties are assumed to be fully correlated among all signal regions with $N_{\text{jet}} = 0$ and $= 1$. A relative sign between two entries in a column indicates anti-correlation between those signal regions for that source of uncertainty.

Channel	Range (GeV)	QCD scale (%)	PS, UE (%)	PDF (%)	Modelling (%)
$N_{\text{jet}} = 0$					
$e\mu + \mu e$	$10 < m_{\ell\ell} < 30$	0.9	0.2	1.5	−1.2
$e\mu + \mu e$	$30 \leq m_{\ell\ell} < 50$	0.9	0.8	1.1	−1.4
$ee + \mu\mu$	$12 < m_{\ell\ell} < 50$	1.0	0.3	1.1	1.7
$N_{\text{jet}} = 1$					
$e\mu + \mu e$	$10 < m_{\ell\ell} < 30$	1.6	0.5	2.0	−5.1
$e\mu + \mu e$	$30 \leq m_{\ell\ell} < 50$	1.5	0.5	1.8	−5.0
$ee + \mu\mu$	$12 < m_{\ell\ell} < 50$	1.4	0.6	1.7	−3.1

Ref. [61]. Four main sources of uncertainty on the normalisation have been considered: QCD renormalisation and factorisation scales, dependence on PDF, dependence on the choice of Monte Carlo generator, and dependence on the UE and PS model. Scale uncertainties have been computed using the MCFM generator by varying the renormalisation and factorisation scales by a factor of 2 while keeping their ratio between them between 0.5 and 2. PDF uncertainties are calculated as for the signal, using the same generator as used for the central value of α.

The signal extraction procedure relies on the precise knowledge of the modelling by simulation. These uncertainties are evaluated by comparing the α from P +P 8 and MCFM. MC@NLO is not included in this comparison because the calculation excludes singly-resonant processes and does not treat spin correlations at the matrix element level. The UE and PS uncertainties are evaluated by comparing the predictions of P interfaced with P 8, P 6, and H . The α are found to be positively correlated between $N_{\text{jet}} = 0$ and $= 1$, as well as for all of subdivisions of the signal region by lepton flavour and $m_{\ell\ell}$. The total quoted uncertainties are about 2% and 4–6% for the $N_{\text{jet}} = 0$ and $= 1$ signal regions, respectively. These values are summarised in Table 5. The modelling and scale uncertainties have been checked using aMC@NLO [70, 71], which gives the same results within the statistical uncertainties of the comparison.

Because the m_{T} distribution is used in the analysis to estimate the signal yield, an additional theoretical uncertainty is evaluated on the shape of this distribution for the dominant WW background. It is computed by comparing the m_{T} shape predicted by the MCFM, S , P +P 6, and MC@NLO+H generators, as well as a comparison among showering algorithms. The resulting maximal variations in the normalised m_{T} distributions are about 20% and are concentrated in the tails of the distribution. The envelope of the distributions from the comparison, which is dominated by the differences between MCFM and MC@NLO+H , is taken as a relative shape uncertainty on the P m_{T} distribution.

The dominant uncertainties on the top background for the $N_{\text{jet}} = 0$ analysis are the theoretical uncertainties on the component derived from MC simulation. These total to 10% and include the effects of QCD scale, initial- and final-state radiation, generator/PS model, the relative normalisation of $t\bar{t}$ and single top, and the interference between single top and $t\bar{t}$, which is neglected when using

separate $t\bar{t}$ and single top Monte Carlo samples. The top background for $N_{\text{jet}} = 1$ and ≥ 2 is evaluated by extrapolation from a signal-depleted CR, as is the case for WW, but the associated uncertainty is dominated by experimental uncertainties, to be described in the next section. For $N_{\text{jet}} = 1$, the uncertainty of 8% on α is evaluated by comparison of simulated $t\bar{t}$ and single top events with different QCD tunes for initial- and final-state radiation. For $N_{\text{jet}} \geq 2$, the uncertainty of 15% on α is evaluated by comparing the modelling of various generators after the VBF-related selection.

The WW yield in $N_{\text{jet}} \geq 2$ is predicted by simulation. Two types of contributions are considered: QCD processes with gluon emissions and electroweak processes without. For the former, a total uncertainty of 42% is dominated by QCD scale and PDF variations. For the latter, which are non-negligible in $N_{\text{jet}} \geq 2$ channel, a total uncertainty of 11% is obtained by considering the QCD scale, the interference between QCD and Higgs processes, and the difference between the S and MadGraph generators.

5.3 Experimental uncertainties

The experimental uncertainties affect both the expected signal and background yields, and are primarily associated with the reconstruction efficiency and energy/momentum scale and resolution of the different objects (leptons, jets, and $E_{\text{T}}^{\text{miss}}$) in the event. The most significant contributions are from the jet energy scale and resolution, the b-tagging efficiency, and the 30% uncertainty on the fake factor used to calculate the W+ jets background. The uncertainty on the integrated luminosity is 3.6%. It is derived, following the methodology of Ref. [72], from a preliminary calibration of the luminosity scale derived from beam-separation scans of April 2012.

The jet energy scale is determined from a combination of test beam, simulation, and *in situ* measurements. Its uncertainty is split into several independent components: η intercalibration of jets from the central to the forward region, high-p_{T} jets, MC non-closure, topologies with close-by jets, different quark/gluon composition and response, the b-jet energy scale, impact from in-time and out-of-time event pile-up, and *in situ* jet energy corrections. The latter is further divided into several different categories depending on the physical source of the uncertainty. The jet energy scale uncertainty, for jets with $p_{\text{T}} > 25\,\text{GeV}$ and $|\eta| < 4.5$, is 1–5% depending on p_{T} and η. The jet energy resolution varies from 5% to 20% as a function of the jet p_{T} and η. The relative uncertainty on the resolution, as determined from *in situ* measurements, ranges from 2% to 40%, with the largest value of the resolution and relative uncertainty occurring at the p_{T} threshold of the jet selection. The reconstruction, identification, and trigger efficiencies for electrons and muons, as well as their momentum scales and resolutions, are estimated using $Z \to \ell\ell$, $J/\psi \to \ell\ell$, and $W \to \ell\nu$ decays ($\ell = e, \mu$). With the exception of the uncertainty on the electron selection efficiency, which varies between 2% and 5% as a function of p_{T} and η, the resulting uncertainties are all smaller than 1%.

The efficiency of the b-tagging algorithm is calibrated using samples containing muons reconstructed in the vicinity of jets [58]. The resulting uncertainty on the b-jet tagging efficiency varies between 5% and 12% as a function of jet p_{T}.

The changes in jet energy and lepton energy/momentum due to systematic variations are propagated to $E_{\text{T}}^{\text{miss}}$ and $E_{\text{T,STVF}}^{\text{miss}}$; the changes in the high-p_{T} object energy/momentum and in the $E_{\text{T}}^{\text{miss}}$ quantities are, therefore, fully correlated. Additional contributions to the $E_{\text{T}}^{\text{miss}}$ and $E_{\text{T,STVF}}^{\text{miss}}$ uncertainty arise from jets with $p_{\text{T}} < 20\,\text{GeV}$ as well as from low-energy calorimeter deposits not associated with reconstructed physics objects [55]; their effect on the total signal and background yields is about 3%.

Lepton momentum scale uncertainties are also propagated to the $p_{\text{T}}^{\text{miss}}$ calculation. In addition, uncertainties are assigned to the scale and resolution of the remaining $p_{\text{T}}^{\text{miss}}$ component not associated

Table 6: Total relative uncertainties on backgrounds that are normalised using control regions (CR). The statistical component (Stat.) is from the CR yields; the theoretical uncertainties (Theory) are from the α extrapolation parameter; the experimental (Expt.) uncertainties are given. The approximate uncertainties on the normalisation of other processes in the CR (Crosstalk) are given. The WW and top in $N_{\text{jet}} = 1$ are anti-correlated due to the b-jet selection, so that the uncertainties partially cancel.

Estimate	Stat. (%)	Theory (%)	Expt. (%)	Crosstalk (%)	Total (%)
WW					
$N_{\text{jet}} = 0$	2.9	1.6	4.4	5.0	7.4
$N_{\text{jet}} = 1$	6	5	4	36	37
Top					
$N_{\text{jet}} = 1$	2	8	22	16	29
$N_{\text{jet}} \geq 2$	10	15	29	19	39

with charged leptons. These uncertainties are calculated by comparing the properties of $p_{\text{T}}^{\text{miss}}$ in Z events in real and simulated data, as a function of the sum of the hard p_{T} objects in the event.

In the fit to the m_{T} distribution to extract the signal yield, the predicted m_{T} shape from simulation is used for all of the backgrounds except $W+$ jets. For $W+$ jets, the shape is taken from the same data which is used to normalise the background estimate, with the same fake factor applied. For the other backgrounds, the impact of experimental uncertainties on the m_{T} shapes for the individual backgrounds and signal are evaluated, and no statistically significant dependence is observed for the majority of the experimental uncertainties. Those experimental uncertainties which do produce statistically significant variations of the shape have no appreciable effect on the final results, because the uncertainty on the m_{T} shape of the total background is dominated by the uncertainties on the normalisations of the individual backgrounds.

5.4 Uncertainties on backgrounds normalised to control regions

For the backgrounds normalised using CRs (WW for the $N_{\text{jet}} = 0$ and $N_{\text{jet}} = 1$ analyses and top in the $N_{\text{jet}} = 1$ and ≥ 2 analyses), the sources of uncertainty can be grouped into four categories: the statistical uncertainty, the theoretical and experimental uncertainties on the simulation-based extrapolation from the CR to the signal region, and the uncertainty on the other contributing processes in the CR, which are subtracted from the data yield to get the estimated number of events from the targeted background. These four sources, and the resulting total uncertainty, are summarised in Table 6. The uncertainties on α are described above, and the statistical uncertainty is derived from the number of events in the corresponding CR, which can be found in Table 4. The uncertainties from the normalisation of other processes in the CR, as represented here, are necessarily approximate because of the correlations among the backgrounds, but the correlations are fully represented in the fit to the data used to extract the results.

6 Re-analysis of 7 TeV data

The 7 TeV data have re-analysed with respect to Ref. [73] to exploit the improvements developed for the analysis of the 8 TeV data, thus facilitating the combination of the results from these two data sets. The object and event selections closely follow Section 3. The largest improvement with respect to

Table 7: Summary selection table for 7 TeV data. The observed (N_{obs}) and the expected (N_{exp}) yields for the signal (N_{sig}) and background (N_{bkg}) processes are given in the m_{T} range noted in Section 3.5. The composition of N_{bkg} is given on the right. The $e\mu + \mu e$ and $ee + \mu\mu$ channels are combined. The N_{sig} sums the ggF and VBF contributions. The selection modifications with respect to Table 2 are discussed in Section 6. The uncertainty on N_{bkg} accounts for the correlations among the sources.

N_{jet}	N_{obs}	N_{bkg}	N_{sig}	N_{WW}	N_{VV}	$N_{t\bar{t}}$	N_t	N_{Z/γ^*}	$N_{W+\text{jets}}$
= 0	154	161 ± 11	25 ± 5	113 ± 10	12 ± 2	5 ± 1	4 ± 1	6 ± 2	21 ± 5
= 1	62	47 ± 6	7 ± 2	16 ± 6	5 ± 1	10 ± 3	6 ± 2	5 ± 2	5 ± 1
≥ 2	2	4.6 ± 0.8	1.4 ± 0.2	0.7 ± 0.2	-	0.7 ± 0.5	0.1 ± 0.1	2.4 ± 0.6	0.3 ± 0.1

Ref. [73] is a 40% reduction of the W+ jets contribution. This is accomplished by tightening the lepton isolation requirement. Other differences include the change in the WW generator and the background estimation techniques to mimic Section 4. P 6 is used for underlying event and parton shower. Due to the lower pile-up conditions during the 7 TeV period, the JVF selection is loosened and the selection in the $ee + \mu\mu$ channels is optimised to accommodate for the lower levels of the DY with respect to 2012.

Figure 8 shows the expected and observed m_{T} distribution of events passing all of the selection for $N_{\text{jet}} = 0$ and = 1 (equivalent to Fig. 4 for 8 TeV). The corresponding plots for $N_{\text{jet}} \geq 2$ are omitted due to limited statistics. Table 7 summarises the predicted signal and backgrounds for events after the selection in the m_{T} ranges described in Section 3.5 (equivalent to Table 11 for 8 TeV). The predicted yields include the statistical and systematic uncertainties.

7 Results

The selection yields and the statistical interpretations are presented. First, the comparison of observed and expected signal and background yields is given in Section 7.1. Second, the statistical method for the signal extraction procedure is described in Section 7.2. Then the statistical interpretation of the combined 7 and 8 TeV results is given in Section 7.3; the VBF interpretation is given in Section 7.3.1. Finally, the interpretations of 7 and 8 TeV results are given in Section 7.4 and Section 7.5, respectively. The discussion of 8 TeV results includes the measurement of the Higgs production cross section.

7.1 Expected signal and background event yields

The expected signal and background yields in the signal regions of the 8 TeV $N_{\text{jet}} = 0$, = 1, and ≥ 2 modes are given in Tables 8, 9, and 10, respectively. The tables show the expected and observed event yields at various stages of the selection. After the selection, the dominant background in the $N_{\text{jet}} = 0$ channel is the continuum WW production with smaller contributions from top, VV, and W+ jets events. In the $N_{\text{jet}} \geq 1$ modes, the contributions from the WW and top processes are comparable. In general, an excess of events relative to the total background is seen. Figure 4 shows the distributions of the transverse mass after the selection.

The summary of the observed and expected yields for the signal and background processes after the selection is given in Table 11. These yields are for the events in the m_{T} ranges specified in Section 3.5, while the full range is used for the fit procedure described below. The VBF process contributes 2%, 12%, and 81% of the signal events expected in the signal region of the $N_{\text{jet}} = 0$, = 1,

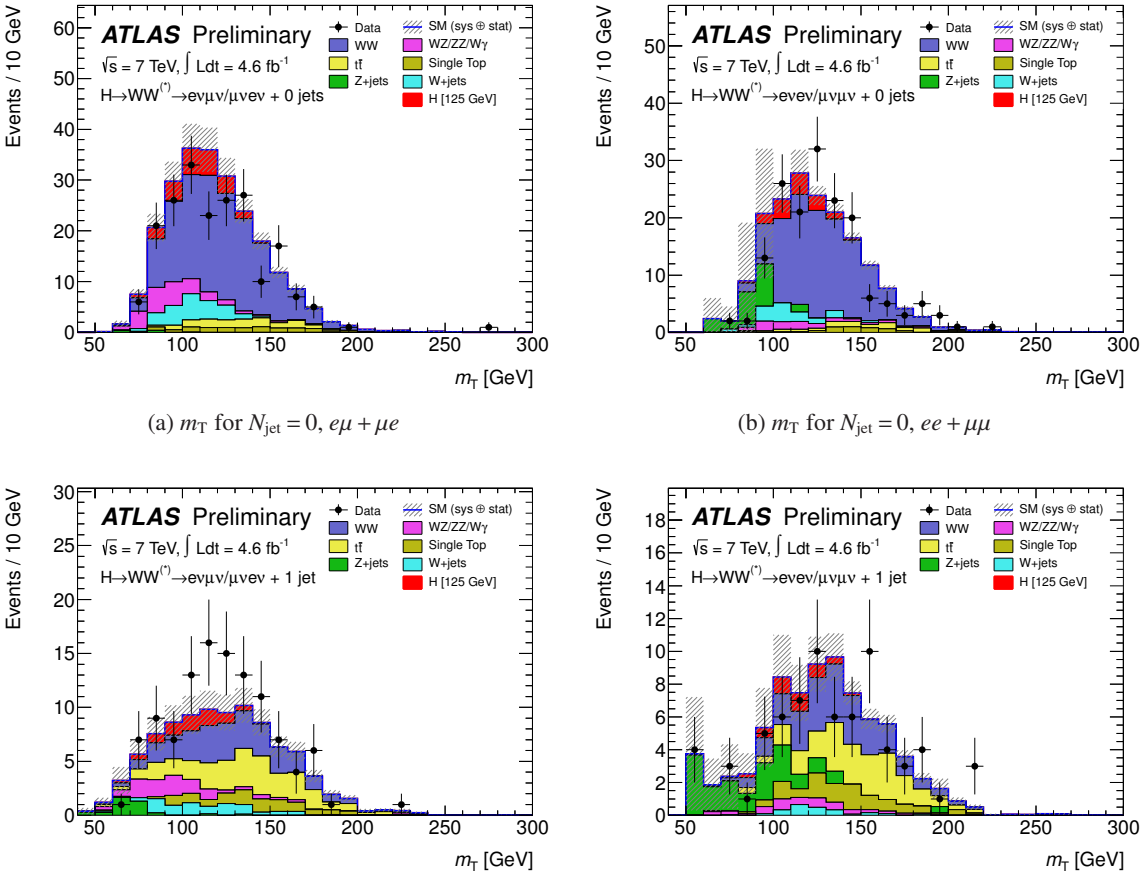

(a) m_{T} for $N_{\mathrm{jet}} = 0$, $e\mu + \mu e$

(b) m_{T} for $N_{\mathrm{jet}} = 0$, $ee + \mu\mu$

(c) m_{T} for $N_{\mathrm{jet}} = 1$, $e\mu + \mu e$

(d) m_{T} for $N_{\mathrm{jet}} = 1$, $ee + \mu\mu$

Figure 8: Distribution of transverse mass, m_{T}, for 7 TeV data. The plots are shown for the $e\mu + \mu e$ (left) and $ee + \mu\mu$ (right) channels in the $N_{\mathrm{jet}} = 0$ (top) and $N_{\mathrm{jet}} = 1$ (bottom) modes. The visible signal is stacked on top of the background. The shaded area represents the uncertainty on the signal and background yields from statistical, experimental, and theoretical sources. Table 2 lists the selection order and Section 6 describes the modifications made with respect to the 8 TeV analysis.

and ≥ 2 analyses, respectively. The uncertainties in the table include the systematic uncertainties discussed in Section 5, and correspond to those entering the statistical procedure described next. The total uncertainty on the background is calculated accounting for the correlations among the individual backgrounds and includes all contributions.

The main sources of systematic uncertainties are summarised in Table 12. As done for Table 11, the values are for events in the m_{T} range. Moreover, the constraints from control regions are included. The uncertainties are shown by source rather than by their impact on the signal or a particular background. For example, the jet energy scale and resolution affect the signal and backgrounds in a correlated way, but only their impact on the total signal and background expectations is shown.

The distribution of m_{T} after the $N_{\mathrm{jet}} = 0$ and $= 1$ selection after subtracting the background is shown in Figure 9. The distribution is similar to that of the signal.

Table 8: Selection table for $N_{\text{jet}} = 0$ in 8 TeV data. The observed (N_{obs}) and expected (N_{exp}) yields for the signal (N_{sig}) and background (N_{bkg}) processes are shown for the (a) $e\mu + \mu e$ and (b) $ee + \mu\mu$ channels. The composition of N_{bkg} is given on the right. The requirements are imposed sequentially from top to bottom. Energies, masses, and momenta are in units of GeV. All uncertainties are statistical.

(a) $e\mu + \mu e$ channel

Selection	N_{obs}	N_{bkg}	N_{sig}	N_{WW}	N_{VV}	$N_{t\bar{t}}$	N_t	N_{Z/γ^*}	$N_{W+\text{jets}}$
$N_{\text{jet}} = 0$	9024	9000 ± 40	172 ± 2	4900 ± 20	370 ± 10	510 ± 10	310 ± 10	2440 ± 30	470 ± 10
$\lvert\Delta\phi_{\ell\ell,MET}\rvert > \frac{\pi}{2}$	8100	8120 ± 40	170 ± 2	4840 ± 20	360 ± 10	490 ± 10	310 ± 10	1690 ± 30	440 ± 10
$p_{\text{T}}^{\ell\ell} > 30$	5497	5490 ± 30	156 ± 2	4050 ± 20	290 ± 10	450 ± 10	280 ± 10	100 ± 10	320 ± 5
$m_{\ell\ell} < 50$	1453	1310 ± 10	124 ± 1	960 ± 10	110 ± 6	69 ± 3	46 ± 3	18 ± 7	100 ± 2
$\lvert\Delta\phi_{\ell\ell}\rvert < 1.8$	1399	1240 ± 10	119 ± 1	930 ± 10	107 ± 6	67 ± 3	44 ± 3	13 ± 7	88 ± 2

(b) $ee + \mu\mu$ channel

Selection	N_{obs}	N_{bkg}	N_{sig}	N_{WW}	N_{VV}	$N_{t\bar{t}}$	N_t	N_{Z/γ^*}	$N_{W+\text{jets}}$
$N_{\text{jet}} = 0$	16446	15600 ± 200	104 ± 1	2440 ± 10	190 ± 5	280 ± 6	175 ± 6	12300 ± 160	170 ± 10
$\lvert\Delta\phi_{\ell\ell,MET}\rvert > \frac{\pi}{2}$	13697	12970 ± 140	103 ± 1	2430 ± 10	190 ± 5	280 ± 6	174 ± 6	9740 ± 140	160 ± 10
$p_{\text{T}}^{\ell\ell} > 30$	5670	5650 ± 70	99 ± 1	2300 ± 10	170 ± 5	260 ± 6	167 ± 5	2610 ± 70	134 ± 4
$m_{\ell\ell} < 50$	2314	2390 ± 20	84 ± 1	760 ± 10	64 ± 3	53 ± 3	42 ± 3	1410 ± 20	62 ± 3
$p_{\text{T,rel}}^{\text{miss}} > 45$	1032	993 ± 10	63 ± 1	650 ± 10	42 ± 2	47 ± 3	39 ± 3	200 ± 5	19 ± 2
$\lvert\Delta\phi_{\ell\ell}\rvert < 1.8$	1026	983 ± 10	63 ± 1	640 ± 10	41 ± 2	46 ± 3	39 ± 3	195 ± 5	18 ± 2
$f_{\text{recoil}} < 0.05$	671	647 ± 7	42 ± 1	520 ± 10	30 ± 2	19 ± 2	22 ± 2	49 ± 3	12 ± 1

Table 9: Selection table for $N_{\text{jet}} = 1$ in 8 TeV data. More details are given in the caption of Table 8.

(a) $e\mu + \mu e$ channel

Selection	N_{obs}	N_{bkg}	N_{sig}	N_{WW}	N_{VV}	$N_{t\bar{t}}$	N_t	N_{Z/γ^*}	$N_{W+\text{jets}}$
$N_{\text{jet}} = 1$	9527	9460 ± 40	97 ± 1	1660 ± 10	270 ± 10	4980 ± 30	1600 ± 20	760 ± 20	195 ± 5
$N_{b\text{-jet}} = 0$	4320	4240 ± 30	85 ± 1	1460 ± 10	220 ± 10	1270 ± 10	460 ± 10	670 ± 10	160 ± 4
$Z \to \tau\tau$ veto	4138	4020 ± 30	84 ± 1	1420 ± 10	220 ± 10	1220 ± 10	440 ± 10	580 ± 10	155 ± 4
$m_{\ell\ell} < 50$	886	830 ± 10	63 ± 1	270 ± 4	69 ± 5	216 ± 6	80 ± 4	149 ± 5	46 ± 2
$\lvert\Delta\phi_{\ell\ell}\rvert < 1.8$	728	650 ± 10	59 ± 1	250 ± 4	60 ± 4	204 ± 6	76 ± 4	28 ± 3	34 ± 2

(b) $ee + \mu\mu$ channel

Selection	N_{obs}	N_{bkg}	N_{sig}	N_{WW}	N_{VV}	$N_{t\bar{t}}$	N_t	N_{Z/γ^*}	$N_{W+\text{jets}}$
$N_{\text{jet}} = 1$	8354	8120 ± 90	54 ± 1	820 ± 10	140 ± 10	2740 ± 20	890 ± 10	3470 ± 80	60 ± 10
$N_{b\text{-jet}} = 0$	5192	4800 ± 80	48 ± 1	720 ± 10	120 ± 10	720 ± 10	260 ± 10	2940 ± 70	40 ± 10
$m_{\ell\ell} < 50$	1773	1540 ± 20	38 ± 1	195 ± 4	35 ± 2	166 ± 5	65 ± 3	1060 ± 10	20 ± 2
$p_{\text{T,rel}}^{\text{miss}} > 45$	440	420 ± 10	21 ± 1	148 ± 3	21 ± 1	128 ± 5	52 ± 3	64 ± 4	5.1 ± 0.8
$\lvert\Delta\phi_{\ell\ell}\rvert < 1.8$	430	410 ± 10	20 ± 1	143 ± 3	20 ± 1	125 ± 5	51 ± 3	63 ± 4	4.5 ± 0.7
$f_{\text{recoil}} < 0.2$	346	320 ± 10	16 ± 1	128 ± 3	17 ± 1	97 ± 4	44 ± 3	25 ± 2	3.1 ± 0.6

7.2 Statistical model and signal extraction

The statistical analysis uses the likelihood function $\mathcal{L}$, the product of Poisson functions for each signal and control region and Gaussian constraints, where the product is over the decay channels. In the Poisson term for the signal region μ scales the expected signal yield, with $\mu = 0$ corresponding to

Table 10: Selection table for $N_{\text{jet}} \geq 2$ in 8 TeV data. More details are given in the caption of Table 8. In this table, the $N_{\text{sig,ggF}}$ is included in N_{bkg}; the $N_{\text{sig},VH}$ is included in $N_{\text{sig,VBF}}$, but the contributions are negligible after the VBF-related criteria. The y gap is described in Table 2.

(a) $e\mu + \mu e$ channel

Selection	N_{obs}	N_{bkg}	$N_{\text{sig,VBF}}$	$N_{\text{sig,ggF}}$	N_{WW}	N_{VV}	$N_{t\bar{t}}$	N_t	N_{Z/γ^*}	$N_{W+\text{jets}}$
$N_{\text{jet}} \geq 2$	48723	47740 ± 80	43 ± 1	67 ± 1	940 ± 10	300 ± 20	41800 ± 70	2370 ± 20	1800 ± 30	440 ± 10
$N_{b\text{-jet}} = 0$	5852	5690 ± 30	31 ± 1	49 ± 1	690 ± 10	200 ± 10	2930 ± 20	350 ± 10	1300 ± 20	171 ± 5
$p_{\text{T}}^{\text{tot}} < 45$	4790	4620 ± 30	27 ± 1	41 ± 1	590 ± 10	160 ± 10	2320 ± 20	290 ± 10	1100 ± 20	126 ± 4
$Z \to \tau\tau$ veto	4007	3840 ± 30	25 ± 1	38 ± 1	540 ± 10	140 ± 10	2150 ± 20	260 ± 10	600 ± 20	108 ± 4
$\lvert\Delta y_{jj}\rvert > 2.8$	696	680 ± 10	12 ± 0.2	9.5 ± 0.3	100 ± 2	25 ± 3	380 ± 10	55 ± 3	95 ± 5	19 ± 2
$m_{jj} > 500$	198	170 ± 4	7.5 ± 0.1	2.9 ± 0.2	34 ± 1	5.6 ± 0.6	93 ± 3	11 ± 1	19 ± 2	4.4 ± 0.7
No jets in y gap	92	77 ± 2	6.3 ± 0.1	1.7 ± 0.2	25 ± 1	2.8 ± 0.4	30 ± 2	5.2 ± 0.8	9 ± 1	3.1 ± 0.6
Both ℓ in y gap	78	59 ± 2	6.1 ± 0.1	1.6 ± 0.1	19 ± 1	2.1 ± 0.3	22 ± 1	4.3 ± 0.7	7 ± 1	2.4 ± 0.5
$m_{\ell\ell} < 60$	31	16 ± 1	5.5 ± 0.1	1.5 ± 0.1	3.8 ± 0.4	0.7 ± 0.2	4.5 ± 0.7	0.7 ± 0.3	4.4 ± 0.8	1.0 ± 0.4
$\lvert\Delta\phi_{\ell\ell}\rvert < 1.8$	23	12 ± 1	5.1 ± 0.1	1.3 ± 0.1	3.5 ± 0.4	0.6 ± 0.2	3.7 ± 0.7	0.7 ± 0.3	1.9 ± 0.5	0.6 ± 0.3

(b) $ee + \mu\mu$ channel

Selection	N_{obs}	N_{bkg}	$N_{\text{sig,VBF}}$	$N_{\text{sig,ggF}}$	N_{WW}	N_{VV}	$N_{t\bar{t}}$	N_t	N_{Z/γ^*}	$N_{W+\text{jets}}$
$N_{\text{jet}} \geq 2$	32877	32300 ± 100	26 ± 0.7	40 ± 1	540 ± 6	180 ± 10	24540 ± 60	1390 ± 20	5420 ± 90	190 ± 10
$N_{b\text{-jet}} = 0$	65388	6370 ± 80	19 ± 0.6	30 ± 1	390 ± 5	130 ± 10	1750 ± 20	200 ± 10	3810 ± 80	58 ± 4
$p_{\text{T}}^{\text{tot}} < 45$	4903	4830 ± 70	17 ± 0.5	24 ± 1	340 ± 4	92 ± 5	1370 ± 10	170 ± 10	2790 ± 70	43 ± 3
$\lvert\Delta y_{jj}\rvert > 2.8$	958	930 ± 30	8.1 ± 0.2	6.2 ± 0.3	61 ± 2	12 ± 1.3	252 ± 6	35 ± 2	560 ± 30	6 ± 1
$m_{jj} > 500$	298	245 ± 6	5.5 ± 0.1	2.1 ± 0.2	23 ± 1	4.1 ± 1.1	62 ± 3	9 ± 1	142 ± 5	1.4 ± 0.6
No jets in y gap	147	119 ± 4	4.7 ± 0.1	1.1 ± 0.1	17 ± 1	2.8 ± 1.1	19 ± 1	4.1 ± 0.7	74 ± 3	0.7 ± 0.4
Both ℓ in y gap	108	85 ± 3	4.5 ± 0.1	0.9 ± 0.1	12 ± 1	2.3 ± 1.1	14 ± 1	3.1 ± 0.6	51 ± 3	0.3 ± 0.3
$m_{\ell\ell} < 60$	52	40 ± 2	4.0 ± 0.1	0.8 ± 0.1	3.2 ± 0.3	1.6 ± 1.1	3.7 ± 0.6	0.8 ± 0.3	30 ± 2	0.1 ± 0.2
$\lvert\Delta\phi_{\ell\ell}\rvert < 1.8$	42	34 ± 2	3.7 ± 0.1	0.7 ± 0.1	2.8 ± 0.3	1.6 ± 1.1	3.3 ± 0.5	0.7 ± 0.3	25 ± 2	0.1 ± 0.2

Table 11: Summary selection table for 8 TeV data for events in the m_{T} range noted in Section 3.5. The uncertainty on N_{bkg} accounts for the correlations among the sources. More details are given in the caption of Table 7.

N_{jet}	N_{obs}	N_{bkg}	N_{sig}	N_{WW}	N_{VV}	$N_{t\bar{t}}$	N_t	N_{Z/γ^*}	$N_{W+\text{jets}}$
$= 0$	831	739 ± 39	97 ± 20	551 ± 41	58 ± 8	23 ± 3	16 ± 2	30 ± 10	61 ± 21
$= 1$	309	261 ± 28	40 ± 13	108 ± 40	27 ± 6	68 ± 18	27 ± 10	12 ± 6	20 ± 5
≥ 2	55	36 ± 4	10.6 ± 1.4	4.1 ± 1.5	1.9 ± 0.4	4.6 ± 1.7	0.8 ± 0.4	22 ± 3	0.7 ± 0.2

no signal and $\mu = 1$ corresponding to the SM hypothesis. As the parameter of interest it is allowed to move freely to best fit the data. The expected signal and background yields in the Poisson are allowed to vary within the allowed range of the relevant systematic uncertainties. Such an uncertainty is parametrised by the corresponding nuisance parameter θ (its collection is $\boldsymbol{\theta}$) that is constrained by the Gaussian. The parametrisations are implemented as log-normal distributions in order to restrict the nuisance parameters from taking unphysical values.

The signal strength μ is found by maximising $\mathcal{L}$ that is defined using the m_{T} distribution for events after the selections in Tables 8–10. As mentioned in Section 3.5, the samples for the $e\mu + \mu e$ channel in $N_{\text{jet}} \leq 1$ are split at $m_{\ell\ell} = 30$ GeV, treating them as separate signal regions. The full m_{T} distribution is divided into five, three, and four bins for $N_{\text{jet}} = 0$, $= 1$, and ≥ 2, respectively. For $N_{\text{jet}} \leq 1$, the bins are

Table 12: Leading systematic uncertainties on the expected event yields for the 8 TeV analysis. The first four rows are calculated for inclusive N_{jet} modes and redistributed to exclusive ones (Section 5). The QCD scale uncertainties on the inclusive ggF cross sections are anti-correlated between the exclusive N_{jet} modes. Some uncertainties are grouped differently with respect to Table 11 to reflect the treatment of correlations; most experimental ones are correlated between the signal and background. Sources contributing less than 4% to any column, and individual entries below 1%, are omitted.

	Signal processes (%)			Background processes (%)		
Source	$N_{\text{jet}}=0$	$N_{\text{jet}}=1$	$N_{\text{jet}}\geq 2$	$N_{\text{jet}}=0$	$N_{\text{jet}}=1$	$N_{\text{jet}}\geq 2$
Theoretical uncertainties						
QCD scale for ggF signal for $N_{\text{jet}}\geq 0$	13	-	-	-	-	-
QCD scale for ggF signal for $N_{\text{jet}}\geq 1$	10	27	-	-	-	-
QCD scale for ggF signal for $N_{\text{jet}}\geq 2$	-	15	4	-	-	-
QCD scale for ggF signal for $N_{\text{jet}}\geq 3$	-	-	4	-	-	-
Parton shower and UE model (signal only)	3	10	5	-	-	-
PDF model	8	7	3	1	1	1
$H\rightarrow WW$ branching ratio	4	4	4	-	-	-
QCD scale (acceptance)	4	4	3	-	-	-
WW normalisation	-	-	-	1	2	4
Experimental uncertainties						
Jet energy scale and resolution	5	2	6	2	3	7
b-tagging efficiency	-	-	-	-	7	2
f_{recoil} efficiency	1	1	-	4	2	-

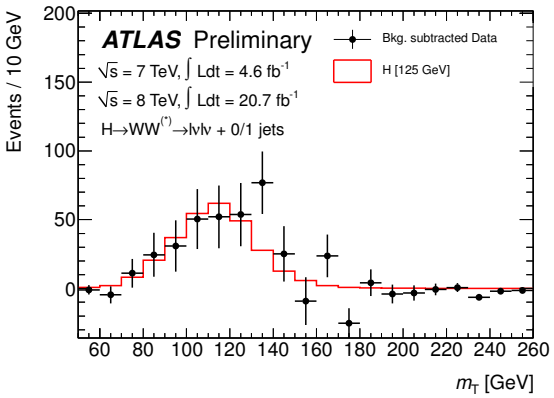

Figure 9: Background-subtracted m_{T} distribution for $N_{\text{jet}}\leq 1$ in 7 and 8 TeV data. The signal is overlaid. The error bars represent the statistical uncertainties of the data and the subtracted background; it does not include the systematic uncertainties of the latter.

of variable widths to have the same number of expected background events in each bin to reduce the effect of MC statistics. For $N_{\text{jet}}\geq 2$, the divisions occur at 50, 80, and 130 GeV for the 8 TeV analysis, and one bin with $m_{\text{T}}<150$ GeV is used for the 7 TeV analysis. The use of the m_{T} distribution relies on the knowledge of its shape, and the effects of those uncertainties are small in comparison to those from the WW normalisation. Interference effects between $gg\rightarrow WW$ and the signal reduce the total expected event yield by about 10% at $m_{\text{T}}\gtrsim m_H$ [74]. The impact on the analysis is negligible because the signal region is binned in m_{T} and the high end of the distribution has a low expected S/B and

contributes relatively little to the sensitivity.

The modified frequentist method known as CL_s [75, 76] is used to compute 95% confidence level (CL) exclusions and the p_0 value. The method uses a test statistic q_μ, a function of μ that depends on the profiled values $\hat{\boldsymbol{\theta}}_\mu$, $\hat{\boldsymbol{\theta}}$, and $\hat{\mu}$: $q_\mu = -2\ln(\mathcal{L}(\mu;\hat{\boldsymbol{\theta}}_\mu)/\mathcal{L}(\hat{\mu};\hat{\boldsymbol{\theta}}))$. The denominator does not depend on μ. The quantities $\hat{\mu}$ and $\hat{\theta}$ are the values of μ and θ, respectively, that unconditionally maximise $\mathcal{L}$. The numerator depends on the values $\hat{\boldsymbol{\theta}}_\mu$ that maximise $\mathcal{L}$ for a given value of μ. For the limit calculation the range of $\hat{\mu}$ is restricted, $0 \leq \hat{\mu} \leq \mu$, so that the results are physical.

The p_0 value, the probability to obtain a value of q_0 larger than the observed value under the background-only hypothesis, is computed with q_μ evaluated at $\mu = 0$. The $\hat{\mu}$ is allowed to be negative, and the correponding q_0 also becomes negative, to be able to quantify downward fluctuations.

The combined results for the 7 and 8 TeV data account for the correlations between the analyses due to common systematic uncertainties. The correlation of all respective nuisance parameters is assumed to be 100% except for those that are statistical in origin or have a different source for the two datasets. Uncorrelated systematics include the statistical component of the jet energy scale calibration and the luminosity uncertainty. The W+ jets systematic uncertainty, and all theoretical uncertainties, are treated as correlated.

In the following sections, the results are reported with the signal significance in units of standard deviation (s.d.) and the corresponding p_0 value, the 95% CL exclusion curves, the signal strength parameter μ, and a two-dimensional plot of μ vs. m_H.

7.3 Combined 7 and 8 TeV results

The expected and observed results are given for 7 and 8 TeV data combining the jet multiplicities. The expected signficance of the signal with $m_H = 125$ GeV is 3.7 s.d. ($p_0 = 1 \times 10^{-4}$). The corresponding observed signficance is 3.8 s.d. ($p_0 = 8 \times 10^{-5}$), but the highest value of 4.1 s.d. ($p_0 = 2 \times 10^{-5}$) occurs at $m_H = 140$ GeV. Figure 10a shows that the p_0 curve is flat around $m_H = 125$ GeV due to limited mass resolution. Figure 10b shows that a Standard Model Higgs boson is expected to be excluded at 95% CL down to a mass of $m_H = 119$ GeV. The observed exclusion is for $m_H > 133$ GeV.

The excess of events is quantified for a signal at $m_H = 125$ GeV by

$$\begin{aligned}\mu_{\text{obs}} &= 1.01 \pm 0.21\,(\text{stat.}) \pm 0.19\,(\text{theo. syst.}) \pm 0.12\,(\text{expt. syst.}) \pm 0.04\,(\text{lumi.}) \\ &= 1.01 \pm 0.31.\end{aligned}$$

Table 13 lists the sources of the uncertainties on μ. The dominant systematic uncertainty is the theoretical uncertainty on the WW background normalisation. Another important contribution is the experimental systematic uncertainty, which is dominated by contributions from the b-tagging efficiency and the jet energy scale and resolution (See Table 12). A significant contribution comes from the normalisation of the signal yield including the uncertainty on the cross section and the branching ratio. This uncertainty has an asymmetric effect on μ, even though the uncertainty on σ_{SM} is close to symmetric, because σ_{SM} appears in the denominator of μ. This uncertainty is reduced compared to the yield uncertainties as shown in Table 12 on the $N_{\text{jet}} = 0$, $= 1$, and ≥ 2 modes because the anti-correlated components mostly cancel. Figure 11a shows that the observed μ vs. m_H is consistent with the expected distribution in the presence of a signal; the μ increases at lower values of m_H due to the decreasing expected $\sigma \cdot \mathcal{B}$ for the signal. Figure 11b shows a scan of the likelihood in the μ-m_H plane; the $H \to WW^{(*)} \to \ell\nu\ell\nu$ result is compared to that of $H \to ZZ^{(*)} \to 4\ell$ [77] and $H \to \gamma\gamma$ [78].

Table 13: Leading uncertainties on the signal strength μ for the combined 7 and 8 TeV analysis.

Category	Source	Uncertainty, up (%)	Uncertainty, down (%)
Statistical	Observed data	+21	−21
Theoretical	Signal yield ($\sigma \cdot \mathcal{B}$)	+12	−9
Theoretical	WW normalisation	+12	−12
Experimental	Objects and DY estimation	+9	−8
Theoretical	Signal acceptance	+9	−7
Experimental	MC statistics	+7	−7
Experimental	W+ jets fake factor	+5	−5
Theoretical	Backgrounds, excluding WW	+5	−4
Luminosity	Integrated luminosity	+4	−4
Total		+32	−29

7.3.1 VBF results and measurement of couplings

Statistical tests of a VBF signal are performed on the 7 and 8 TeV data by considering the ggF signal as part of the background. The test defines μ_{VBF}, the signal strength parameter associated with the VBF process, as the parameter of interest. The ggF signal strength μ_{ggF} is profiled, and is constrained mainly by the $N_{\mathrm{jet}} \leq 1$ signal regions.

The expected VBF signal significance at $m_H = 125$ GeV is 1.6 s.d. ($p_0 = 0.05$). The corresponding observed significance is 2.5 s.d. ($p_0 = 0.007$), but the highest value of 2.5 s.d. ($p_0 = 0.006$) occurs at mass $m_H = 115$ GeV. Figure 12a compares the observed p_0 with the expected distribution in the presence of a signal. The 95% CL exclusion on $\sigma/\sigma_{\mathrm{SM}}$ is shown in Fig. 12b. In the absence of a VBF signal, the expected exclusion is $m_H > 130$ GeV. However, the observed exclusion is $m_H > 147$ GeV. Figure 13 shows μ vs. m_H. The best-fit measured signal strength at $m_H = 125$ GeV is

$$\begin{aligned}\mu_{\mathrm{obs,\,VBF}} &= 1.66 \pm 0.67\,(\mathrm{stat.}) \pm 0.42\,(\mathrm{syst.}) \\ &= 1.66 \pm 0.79.\end{aligned}$$

Similarly, μ_{ggF} has been measured on the 7 and 8 TeV data by considering the VBF signal as part of the background. In this test, μ_{VBF} is constrained mainly by the $N_{\mathrm{jet}} \geq 2$ signal region. The best-fit signal strength at $m_H = 125$ GeV is

$$\begin{aligned}\mu_{\mathrm{obs,\,ggF}} &= 0.82 \pm 0.24\,(\mathrm{stat.}) \pm 0.28\,(\mathrm{syst.}) \\ &= 0.82 \pm 0.36.\end{aligned}$$

A two-dimensional likelihood scan of the signal strength for the ggF and VBF production modes is shown in Fig. 14a. Since the signal strengths in the VBF, WH, and ZH production modes scale with the VH coupling, the three strengths are grouped together. The results are consistent with the expected SM values of unity. Figure 14b shows the likelihood curves for the ratio $\mu_{\mathrm{VBF}+VH}/\mu_{\mathrm{ggF}+t\bar{t}H}$ from the $H \to \gamma\gamma$, $H \to ZZ^{(*)} \to 4\ell$, $H \to \tau\tau$, and $H \to WW^{(*)} \to \ell\nu\ell\nu$ analyses. The branching ratio dependence of the individual channels cancels in the ratio so that the compatibility of the measurements in the various channels can be compared. The $H \to WW^{(*)} \to \ell\nu\ell\nu$ channel has a larger best-fit ratio than the other channels, but is consistent with the $H \to \gamma\gamma$ and $H \to ZZ^{(*)} \to 4\ell$ results at 68% CL.

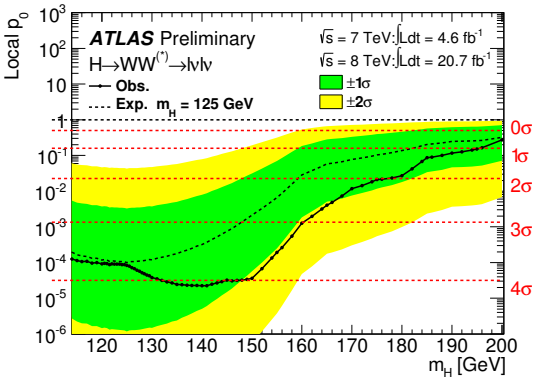

(a) p_0 for observed (solid) and expected (dashed)

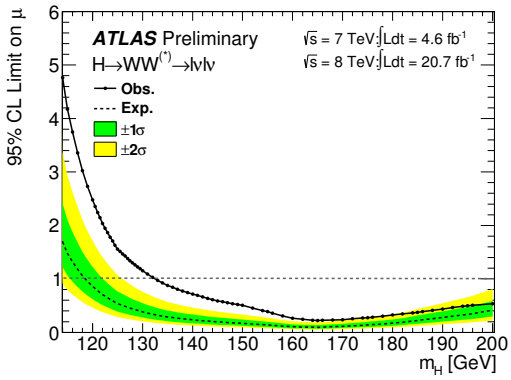

(b) 95% CL upper limit observed (solid) and expected for varying value of m_H corresponding to the x-axis (dashed)

Figure 10: Results for (a) p_0 and (b) 95% CL upper limit using combined 7 TeV and 8 TeV data. The p_0 is the given probability for the background-only scenario as a function of m_H. The expected 95% CL upper limit is computed in the absence of a signal. The upper limit is on the cross section normalised to the SM cross section. For both figures, the smaller green bands represent $\pm 1\sigma$ uncertainties on the expected values, and the larger yellow bands represent $\pm 2\sigma$ uncertainties.

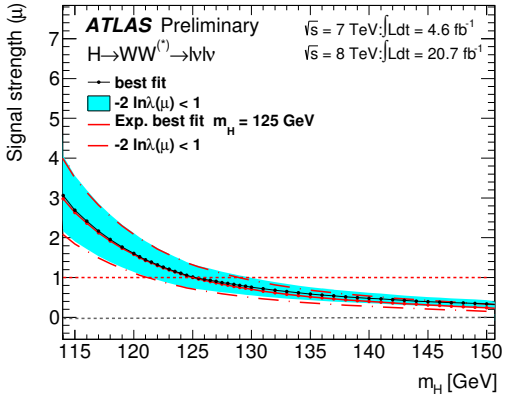

(a) μ value for fitted results (solid black line with shaded cyan band) and the expected result (solid red line with dashed band).

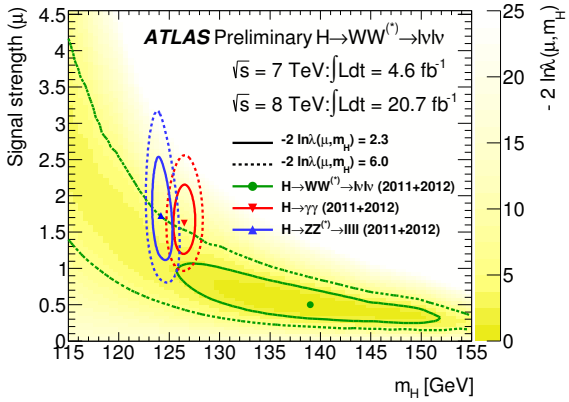

(b) μ vs. m_H likelihood contour. 68% and 95% contours are drawn. $H \to ZZ^{(*)} \to 4\ell$ and $H \to \gamma\gamma$ results are shown. Yellow shading shows $-\ln\lambda(\mu, m_H)$ for $H \to WW^{(*)} \to \ell\nu\ell\nu$.

Figure 11: Signal strength parameter μ vs. m_H: (a) fitted μ value for the given m_H and (b) two-dimensional likelihood contours of $-2\ln\lambda(\mu, m_H)$ in the best-fit signal strength.

7.4 7 TeV results

The expected significance for a Higgs boson at $m_H = 125$ GeV is 1.8 s.d. ($p_0 = 0.04$). The corresponding observed significance is 0 s.d. ($p_0 = 0.5$), which translates into 1.8 s.d. compatibility with a signal at $m_H = 125$ GeV. The highest value of 0.8 s.d. ($p_0 = 0.22$) occurs at $m_H = 158$ GeV.

The best-fit value of the signal strength at $m_H = 125$ GeV is $\mu = 0.0 \pm 0.6$. The result is consistent with the previous result using the 7 TeV data, $\mu = 0.5 \pm 0.7$ at $m_H = 125$ GeV [4].

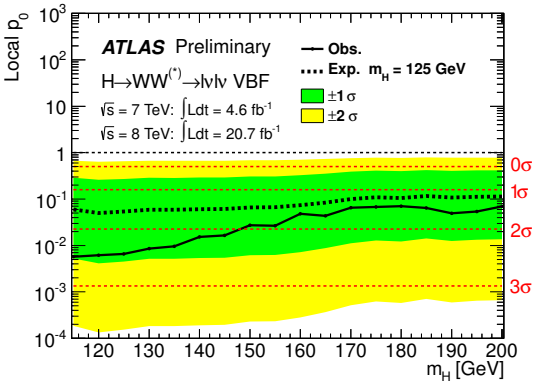

(a) p_0 for observed (solid) and expected (dashed)

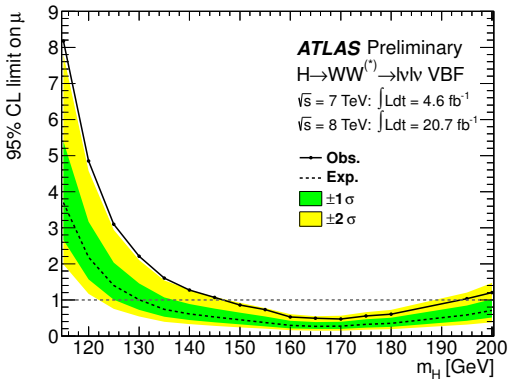

(b) 95% CL upper limit observed (solid) and expected for varying value of m_H corresponding to the x-axis (dashed)

Figure 12: VBF results for (a) p_0 and (b) 95% CL upper limit using 8 TeV data considering VBF as signal and ggF as part of the background. Details are given in the caption of Fig. 10.

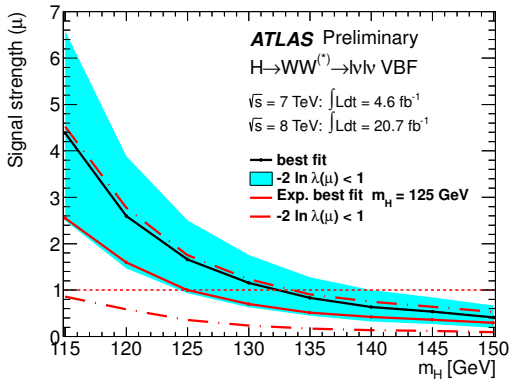

Figure 13: VBF signal strength parameter μ. The observed (solid black line with shaded cyan band) and the expected result (solid red line with dashed band) are shown.

7.5 8 TeV results

The expected significance for the signal with $m_H = 125$ GeV is 3.5 s.d. corresponding to $p_0 = 2 \times 10^{-4}$. The corresponding observed significance is 4.3 s.d. ($p_0 = 1 \times 10^{-5}$), but the highest value of 4.5 s.d. ($p_0 = 4 \times 10^{-6}$) occurs at $m_H = 135$ GeV. The best-fit signal strength μ at $m_H = 125$ GeV is

$$\begin{aligned}\mu_{\text{obs, 8 TeV}} &= 1.26 \pm 0.24\,(\text{stat.}) \pm 0.21\,(\text{theo. syst.}) \pm 0.14\,(\text{expt. syst.}) \pm 0.06\,(\text{lumi.}) \\ &= 1.26 \pm 0.35.\end{aligned}$$

The expected best-fit μ at $m_H = 125$ GeV is

$$\begin{aligned}\mu_{\text{exp}} &= 1 \pm 0.23\,(\text{stat.}) \pm 0.23\,(\text{syst.}) \\ &= 1 \pm 0.33.\end{aligned}$$

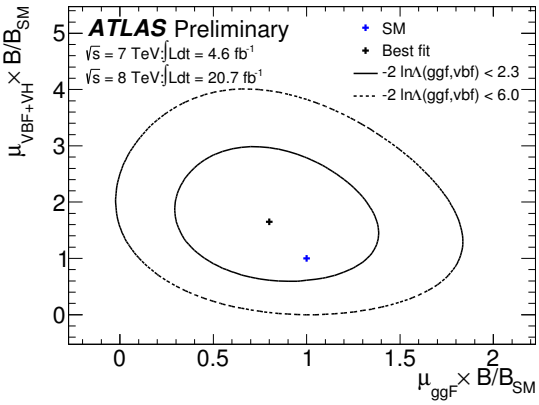

(a) Likelihood contours and best-fit value for $\mu_{\text{ggF+ttH}}$ and $\mu_{\text{VBF+VH}}$. 68% (solid) and 95% (dashed) CL are shown.

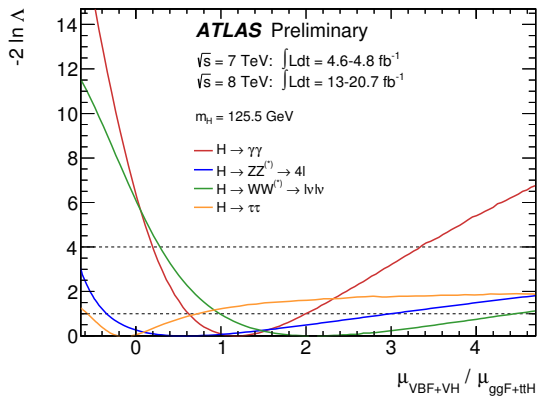

(b) Likelihood curves for the ratio $\mu_{\text{VBF+}VH}/\mu_{\text{ggF+}t\bar{t}H}$ from $H\to\gamma\gamma$, $H\to ZZ^{(*)}\to 4\ell$, $H\to\tau\tau$ and $H\to WW^{(*)}\to\ell\nu\ell\nu$

Figure 14: Likelihood contours for separate ggF and VBF signal strength parameters (a) and the likelihood curves for the ratio of the ggF/VBF strength parameters (b). $H\to WW^{(*)}\to\ell\nu\ell\nu$ analysis uses the combined 7 and 8 TeV data.

The corresponding expected value in Ref. [49] is $1\pm0.32\,(\text{stat.})\pm0.42\,(\text{syst.})$. For both analyses, the systematic uncertainty includes a small but non-negligible contribution from the statistical uncertainty on the analysis inputs derived from simulation. The expected precision is improved relative to Ref. [49] primarily because of the reduced extrapolation uncertainties from the WW control region in $N_{\text{jet}}=0$ and the increase in integrated luminosity. The statistical and systematic uncertainties are comparable in the current analysis.

The observed value of the product of the inclusive cross section $\sigma(pp\to H)$ and branching ratio $\mathcal{B}(H\to WW)$ for a signal at $m_H=125$ GeV—after dividing out the predicted SM cross section, assuming the noted mass for the signal acceptance, and removing the associated uncertainties on the signal yield—is

$$\begin{aligned}(\sigma\cdot\mathcal{B})_{\text{obs, 8 TeV}} &= 6.0\pm1.1\,(\text{stat.})\pm0.8\,(\text{theo. syst.})\pm0.7\,(\text{expt. syst.})\pm0.3\,(\text{lumi.})\,\text{pb}\\ &= 6.0\pm1.6\,\text{pb}.\end{aligned}$$

The corresponding expected value is

$$\begin{aligned}(\sigma\cdot\mathcal{B})_{\text{exp, 8 TeV}} &= 4.8\pm0.6\,(\text{cross section})\pm0.2\,(\text{branching ratio})\,\text{pb}\\ &= 4.8\pm0.7\,\text{pb}.\end{aligned}$$

The expected value is slightly smaller than the observed value, but they are consistent within the uncertainties.

The predicted value of $\sigma\cdot\mathcal{B}$ has been computed as the sum of the values reported in Ref. [61] (updated in Ref. [79]) for the production modes (ggF, VBF, and VH) used to evaluate the signal acceptance. The associated theoretical uncertainties are added linearly following the prescription in Ref. [79].

A cross-check of the results has been done using the yields in the m_{T} ranges described in Section 3.5 in lieu of the distribution. Table 11 gives the corresponding event yields and the uncertainties.

The expected significance for the signal at $m_H = 125\,\text{GeV}$ is lower at 3.3 s.d. ($p_0 = 4 \times 10^{-4}$). The corresponding observed significance is 4.0 s.d. ($p_0 = 3 \times 10^{-5}$).

A statistical test comparing the 7 and 8 TeV results show that they are compatible within 1.8 s.d.

8 Conclusion

The analysis of the $H \to WW^{(*)} \to \ell\nu\ell\nu$ process in the mass range of 115–200 GeV is presented using the complete data sample of 2012 and 2011. The samples correspond, respectively, to 20.7fb^{-1} at $\sqrt{s} = 8\,\text{TeV}$ and 4.6fb^{-1} at 7 TeV collected with the ATLAS detector at the LHC.

An excess of events over the expected background is observed for $m_H \lesssim 150\,\text{GeV}$ with the largest significance of 4.1 standard deviations ($p_0 = 2 \times 10^{-5}$) at $m_H = 140\,\text{GeV}$. The signal significance at $m_H = 125\,\text{GeV}$ is 3.8 standard deviations ($p_0 = 8 \times 10^{-5}$); the best fit signal strength at that mass is $\mu = 1.01 \pm 0.31$.

The measured value of the product of the cross section and the $WW^{(*)}$ branching ratio for a signal at $m_H = 125\,\text{GeV}$ at 8 TeV is $6.0 \pm 1.6\,\text{pb}$ while the expected value is $4.8 \pm 0.7\,\text{pb}$. The results are consistent with the predictions for the Standard Model Higgs boson decaying to a pair of W bosons.

References

[1] F. Englert and R. Brout, *Broken symmetry and the mass of gauge vector mesons*, Phys. Rev. Lett. **13** (1964) 321–323.

[2] P. W. Higgs, *Broken symmetries and the masses of gauge bosons*, Phys. Rev. Lett. **13** (1964) 508–509.

[3] G. Guralnik, C. Hagen, and T. Kibble, *Global conservation laws and massless particles*, Phys.Rev.Lett. **13** (1964) 585–587.

[4] ATLAS Collaboration, *Observation of a new particle in the search for the Standard Model Higgs boson with the ATLAS detector at the LHC*, Phys. Lett. B **716** (2012) 1–29. 39 p, arXiv:1207.7214 [hep-ph].

[5] CMS Collaboration, *Observation of a new boson at a mass of 125 GeV with the CMS experiment at the LHC*, Phys. Lett. B **716** (2012) 30–61. 59 p, arXiv:1207.7235 [hep-ph].

[6] ATLAS Collaboration, *Observation of an excess of events in the search for the Standard Model Higgs boson in the $H \to WW^{(*)} \to \ell\nu\ell\nu$ channel with the ATLAS detector*, ATLAS-CONF-2012-098, 2012. https://cdsweb.cern.ch/record/1462530.

[7] ATLAS Collaboration, *The ATLAS experiment at the CERN Large Hadron Collider*, JINST **3** (2008) S08003.

[8] A. Bredenstein, A. Denner, S. Dittmaier, and M. Weber, *Precise predictions for the Higgs-boson decay $H \to WW/ZZ \to 4$ leptons*, Phys.Rev. **D74** (2006) 013004, arXiv:hep-ph/0604011 [hep-ph].

[9] A. Bredenstein, A. Denner, S. Dittmaier, and M. Weber, *Radiative corrections to the semileptonic and hadronic Higgs-boson decays $H \to WW/ZZ \to 4$ fermions*, JHEP **0702** (2007) 080, arXiv:hep-ph/0611234.

[10] A. Djouadi, J. Kalinowski, and M. Spira, *HDECAY: A program for Higgs boson decays in the Standard Model and its supersymmetric extension*, Comput. Phys. Commun. **108** (1998) 56, arXiv:hep-ph/9704448.

[11] A. Djouadi, M. Spira, and P. Zerwas, *Production of Higgs bosons in proton colliders: QCD corrections*, Phys.Lett. **B264** (1991) 440–446.

[12] S. Dawson, *Radiative corrections to Higgs boson production*, Nucl.Phys. **B359** (1991) 283–300.

[13] M. Spira, A. Djouadi, D. Graudenz, and P. Zerwas, *Higgs boson production at the LHC*, Nucl.Phys. **B453** (1995) 17–82, arXiv:hep-ph/9504378 [hep-ph].

[14] R. Harlander and W. B. Kilgore, *Next-to-next-to-leading order Higgs production at hadron colliders*, Phys. Rev. Lett. **88** (2002) 201801, arXiv:hep-ph/0201206.

[15] C. Anastasiou and K. Melnikov, *Higgs boson production at hadron colliders in NNLO QCD*, Nucl.Phys. **B646** (2002) 220–256, arXiv:hep-ph/0207004 [hep-ph].

[16] V. Ravindran, J. Smith, and W. L. van Neerven, *NNLO corrections to the total cross-section for Higgs boson production in hadron hadron collisions*, Nucl.Phys. **B665** (2003) 325–366, arXiv:hep-ph/0302135 [hep-ph].

[17] U. Aglietti, R. Bonciani, G. Degrassi, and A. Vicini, *Two loop light fermion contribution to Higgs production and decays*, Phys.Lett. **B595** (2004) 432–441, arXiv:hep-ph/0404071 [hep-ph].

[18] S. Actis, G. Passarino, C. Sturm, and S. Uccirati, *NLO electroweak corrections to Higgs boson production at hadron colliders*, Phys. Lett. B **670** (2008) 12, arXiv:0809.1301 [hep-ph].

[19] S. Catani, D. de Florian, M. Grazzini, and P. Nason, *Soft-gluon re-summation for Higgs boson production at hadron colliders*, JHEP **0307** (2003) 028, arXiv:hep-ph/0306211.

[20] C. Anastasiou, S. Buehler, F. Herzog, and A. Lazopoulos, *Inclusive Higgs boson cross-section for the LHC at 8 TeV*, JHEP **1204** (2012) 004, arXiv:1202.3638 [hep-ph].

[21] D. de Florian and M. Grazzini, *Higgs production at the LHC: updated cross sections at* $\sqrt{s} = 8$ *TeV*, (2012) , arXiv:1206.4133 [hep-ph].

[22] J. Baglio and A. Djouadi, *Higgs production at the LHC*, JHEP **1103** (2011) 055, arXiv:1012.0530 [hep-ph].

[23] P. Bolzoni, F. Maltoni, S.-O. Moch, and M. Zaro, *Higgs production via vector-boson fusion at NNLO in QCD*, Phys.Rev.Lett. **105** (2010) 011801, arXiv:1003.4451 [hep-ph].

[24] M. Ciccolini, A. Denner, and S. Dittmaier, *Strong and electroweak corrections to the production of Higgs+2 jets via weak interactions at the LHC*, Phys. Rev. Lett. **99** (2007) 161803, arXiv:0707.0381 [hep-ph].

[25] M. Ciccolini, A. Denner, and S. Dittmaier, *Electroweak and QCD corrections to Higgs production via vector-boson fusion at the LHC*, Phys. Rev. D **77** (2008) 013002, arXiv:0710.4749 [hep-ph].

[26] K. Arnold et al., *VBFNLO: A parton level Monte Carlo for processes with electroweak bosons*, Comput. Phys. Commun. **180** (2009) 1661, arXiv:0811.4559 [hep-ph].

[27] T. Han and S. Willenbrock, *QCD correction to the* $pp \to WH$ *and* ZH *total cross-sections*, Phys.Lett. **B273** (1991) 167–172.

[28] O. Brein, A. Djouadi, and R. Harlander, *NNLO QCD corrections to the Higgs-strahlung processes at hadron colliders*, Phys.Lett. **B579** (2004) 149–156, arXiv:hep-ph/0307206 [hep-ph].

[29] M. L. Ciccolini, S. Dittmaier, and M. Krämer, *Electroweak radiative corrections to associated WH and ZH production at hadron colliders*, Phys. Rev. D **68** (2003) 073003, arXiv:hep-ph/0306234.

[30] P. Nason and C. Oleari, *NLO Higgs boson production via vector-boson fusion matched with shower in POWHEG*, JHEP **1002** (2010) 037, arXiv:0911.5299 [hep-ph].

[31] T. Sjöstrand, S. Mrenna, and P. Z. Skands, *A brief introduction to PYTHIA 8.1*, Computer Physics Communications **178** (2008) no. 11, 852–867.

[32] T. Sjostrand, S. Mrenna, and P. Z. Skands, *PYTHIA 6.4 physics and manual*, JHEP **0605** (2006) 026, arXiv:hep-ph/0603175.

[33] T. Gleisberg et al., *Event generation with SHERPA 1.1*, JHEP **0902** (2009) 007, arXiv:0811.4622 [hep-ph].

[34] N. Kauer and G. Passarino, *Inadequacy of zero-width approximation for a light Higgs boson signal*, JHEP **1208** (2012) 116, arXiv:1206.4803 [hep-ph].

[35] T. Binoth, M. Ciccolini, N. Kauer and M. Krämer, *Gluon-induced W-boson pair production at the LHC*, JHEP **0612** (2006) 046, arXiv:hep-ph/0611170.

[36] G. Corcella et al., *HERWIG 6: An event generator for hadron emission reactions with interfering gluons (including super-symmetric processes)*, JHEP **0101** (2001) 010.

[37] S. Frixione and B. R. Webber, *Matching NLO QCD computations and parton shower simulations*, JHEP **0206** (2002) 029, arXiv:hep-ph/0204244.

[38] B. P. Kersevan and E. Richter-Was, *The Monte Carlo event generator AcerMC version 2.0 with interfaces to PYTHIA 6.2 and HERWIG 6.5*, TPJU-6/2004, 2004. arXiv:hep-ph/0405247.

[39] J. Alwall et al., *MadGraph/MadEvent v4: The new web generation*, JHEP **0709** (2007) 028, arXiv:0706.2334 [hep-ph].

[40] J. Alwall, M. Herquet, F. Maltoni, O. Mattelaer, and T. Stelzer, *MadGraph 5 : going beyond*, JHEP **1106** (2011) 128, arXiv:1106.0522 [hep-ph].

[41] R. C. Gray, C. Kilic, M. Park, S. Somalwar, and S. Thomas, *Backgrounds to Higgs boson searches from $W\gamma^* \to lvl(l)$ asymmetric internal conversion*, (2011) , arXiv:1110.1368 [hep-ph].

[42] J. M. Butterworth, J. R. Forshaw, and M. H. Seymour, *Multiparton interactions in photoproduction at HERA*, Z. Phys. **C72** (1996) 637, arXiv:hep-ph/9601371.

[43] J. Alwall et al., *Comparative study of various algorithms for the merging of parton showers and matrix elements in hadronic collisions*, Eur. Phys. J. C **53** (2008) 473, arXiv:0706.2569 [hep-ph].

[44] J. M. Campbell and R. K. Ellis, *An update on vector boson pair production at hadron colliders*, Phys. Rev. D **60** (1999) 113006, arXiv:hep-ph/9905386.

[45] H.-L. Lai et al., *New parton distributions for collider physics*, Phys. Rev. D **82** (2010) 074024, arXiv:1007.2241 [hep-ph].

[46] P. M. Nadolsky et al., *Implications of CTEQ global analysis for collider observables*, Phys. Rev. D **78** (2008) 013004, arXiv:0802.0007 [hep-ph].

[47] ATLAS Collaboration, *The ATLAS simulation infrastructure*, Eur. Phys. J. C **70** (2010) 823, arXiv:1005.4568 [physics.ins-det].

[48] S. Agostinelli et al., *GEANT 4, a simulation toolkit*, Nucl. Instrum. Meth. **A506** (2003) 250.

[49] ATLAS Collaboration, *Update of the $H \to WW^{(*)} \to e\nu\mu\nu$ analysis with 13 fb^{-1} of $\sqrt{s} = 8$ data collected with the ATLAS Detector*, ATLAS-CONF-2012-158, 2012. https://cdsweb.cern.ch/record/1493601.

[50] ATLAS Collaboration, *Electron performance measurements with the ATLAS detector using the 2010 LHC proton-proton collision data*, Eur. Phys. J. C **72** (2012) 1909, arXiv:1110.3174 [hep-ex].

[51] ATLAS Collaboration, *Muon reconstruction efficiency in reprocessed 2010 LHC proton-proton collision data recorded with the ATLAS detector*, ATLAS-CONF-2011-063 (2011) . https://cdsweb.cern.ch/record/1345743.

[52] M. Cacciari, G. P. Salam, and G. Soyez, *The anti-k_t jet clustering algorithm*, JHEP **0804** (2008) 063, arXiv:0802.1189 [hep-ex].

[53] M. Cacciari and G. P. Salam, *Pileup subtraction using jet areas*, Phys.Lett. **B659** (2008) 119–126, arXiv:0707.1378 [hep-ph].

[54] ATLAS Collaboration, *Jet energy scale and its systematic uncertainty in proton-proton collisions at $\sqrt{s} = 7$ TeV with ATLAS 2011 data*, ATLAS-CONF-2013-004 (2013) .

[55] ATLAS Collaboration, *Performance of missing transverse momentum reconstruction in proton-proton collisions at 7 TeV with ATLAS*, Eur. Phys. J. C **72** (2012) 1844, arXiv:1108.5602 [hep-ex].

[56] ATLAS Collaboration, *Performance of missing transverse momentum reconstruction in ATLAS with 2011 proton-proton collisions at $\sqrt{s} = 7$ TeV*, ATLAS-CONF-2012-101 (2012) .

[57] ATLAS Collaboration, *Commissioning of the ATLAS high-performance b-tagging algorithms in the 7 TeV collision data*, ATLAS-CONF-2011-102 (2011) . https://cdsweb.cern.ch/record/1369219.

[58] ATLAS Collaboration, *Measurement of the b-tag efficiency in a sample of jets containing muons with 5 fb^{-1} of data from the ATLAS detector*, ATLAS-CONF-2012-043 (2012) . https://cdsweb.cern.ch/record/1435197.

[59] R.K. Ellis et al., *Higgs decay to $\tau^+\tau^-$: A possible signature of intermediate mass Higgs bosons at the SSC*, Nucl. Phys. B **297** (1988) 221.

[60] LHC Higgs Cross Section Working Group, S. Dittmaier, C. Mariotti, G. Passarino, and R. Tanaka (Eds.), *Handbook of LHC Higgs Cross Sections: 1. Inclusive Observables*, CERN-2011-002 (CERN, Geneva, 2011) , arXiv:1101.0593 [hep-ph].

[61] LHC Higgs Cross Section Working Group, S. Dittmaier, C. Mariotti, G. Passarino, and R. Tanaka (Eds.), *Handbook of LHC Higgs Cross Sections: 2. Differential Distributions*, CERN-2012-002 (CERN, Geneva, 2012) , arXiv:1201.3084 [hep-ph].

[62] I. Stewart and F. Tackmann, *Theory uncertainties for Higgs mass and other searches using jet bins*, Phys. Rev. D **85** (2012) 034011, arXiv:1107.2117 [hep-ph].

[63] S. Catani and M. Grazzini, *An NNLO subtraction formalism in hadron collisions and its application to Higgs boson production at the LHC*, Phys. Rev. Lett. **98** (2007) 222002, arXiv:hep-ph/0703012.

[64] M. Grazzini, *NNLO predictions for the Higgs boson signal in the $H \to WW \to lvlv$ and $H \to ZZ \to 4l$ decay channels*, JHEP **0802** (2008) 043, arXiv:0801.3232 [hep-ph].

[65] ATLAS and CMS Collaborations, *Procedure for the LHC Higgs boson search combination in summer 2011*, ATL-PHYS-PUB-2011-011, CMS-NOTE-2011-005 (2011) . https://cdsweb.cern.ch/record/1375842.

[66] J. M. Campbell, R. K. Ellis, and C. Williams, *Hadronic production of a Higgs boson and two jets at next-to-leading order*, Phys.Rev. **D81** (2010) 074023, arXiv:1001.4495 [hep-ph].

[67] M. Botje et al., *The PDF4LHC working group interim recommendations*, (2011) , arXiv:1101.0538 [hep-ph].

[68] A. D. Martin, W. J. Stirling, R. S. Thorne, and G. Watt, *Parton distributions for the LHC*, Eur. Phys. J. C **63** (2009) 189, arXiv:0901.0002 [hep-ph].

[69] R. D. Ball et al., *Impact of heavy quark masses on parton distributions and LHC phenomenology*, Nucl. Phys. B **849** (2011) 296, arXiv:1101.1300 [hep-ph].

[70] R. Frederix, S. Frixione, F. Maltoni and T. Stelzer, *Automation of next-to-leading order computations in QCD: The FKS subtraction*, JHEP **0910** (2009) 003, arXiv:hep-ph/09084272.

[71] V. Hirschi, R. Frederix, S. Frixione, M. V. Garzelli, F. Maltoni and R. Pittau, *Automation of one-loop QCD corrections*, JHEP **1105** (2011) 044, arXiv:hep-ph/11030621.

[72] ATLAS Collaboration, *Improved luminosity determination in pp collisions at $\sqrt{s} = 7$ TeV using the ATLAS detector at the LHC*, arXiv:1302.4393 [hep-ex].

[73] ATLAS Collaboration, *Search for the Standard Model Higgs boson in the $H \to WW^{(*)} \to \ell\nu\ell\nu$ decay mode with 4.7 fb^{-1} of ATLAS data at $\sqrt{s} = 7$* TeV, Phys.Lett. **B716** (2012) 62–81, arXiv:1206.0756 [hep-ex].

[74] J. M. Campbell, R. K. Ellis, and C. Williams, *Gluon-gluon contributions to W+ W- production and Higgs interference effects*, JHEP **1110** (2011) 005, arXiv:1107.5569 [hep-ph].

[75] A.L. Read, *Presentation of search results: the CL_s technique*, J. Phys. G **28** (2002) 2693.

[76] G. Cowan, K. Cranmer, E. Gross, and O. Vitells, *Asymptotic formulae for likelihood-based tests of new physics*, Eur. Phys. J. C **71** (2011) 1554.

[77] ATLAS Collaboration, *Measurements of the properties of the Higgs-like boson in the four lepton decay channel with the ATLAS detector using 25 fb^{-1} of proton-proton collision data*, ATLAS-CONF-2013-013 (2013) . https://cdsweb.cern.ch/record/1523699.

[78] ATLAS Collaboration, *Measurements of the properties of the Higgs-like boson in the two photon decay channel with the ATLAS detector using 25 fb^{-1} of proton-proton collision data*, ATLAS-CONF-2013-012 (2013) . https://cdsweb.cern.ch/record/1523698.

[79] S. Dittmaier, C. Mariotti, G. Passarino and R. Tanaka, *The Higgs Cross Section Working Group web page*, https://twiki.cern.ch/twiki/bin/view/LHCPhysics/CrossSections, 2012.

A Additional Figures

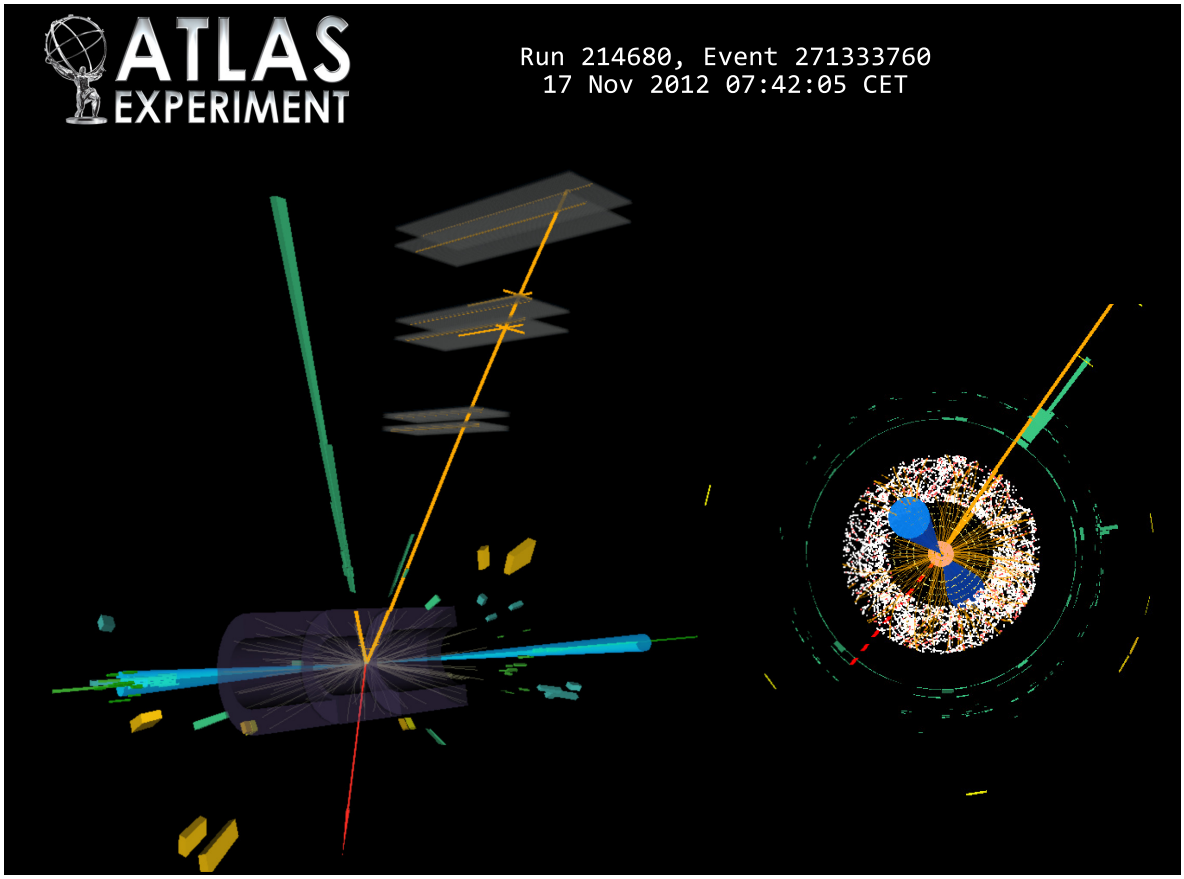

Figure 15: A candidate event for $H \to WW^{(*)} \to e\nu\mu\nu + 2$ jets produced via VBF, $qq \to Hqq$. The event variables are: $m_{jj} = 1.5$ TeV, $|\Delta y_{jj}| = 6.6$, $m_{\ell\ell} = 21$ GeV, and $m_{\mathrm{T}} = 95$ GeV. For the figure on the left (starting from the top left going clockwise): p_{T} of the electron is 51 GeV (thick green line), the muon is 15 GeV (orange line), the jet (right blue cone) is 68 GeV, the $E_{\mathrm{T}}^{\mathrm{miss}}$ (thin dotted red line on the left) is 33 GeV, and the jet (left cyan cone) is 42 GeV. A view transverse to the beam direction is given on the right; previous descriptions of various objects apply except for $E_{\mathrm{T}}^{\mathrm{miss}}$, which is represented as a thick dotted line.

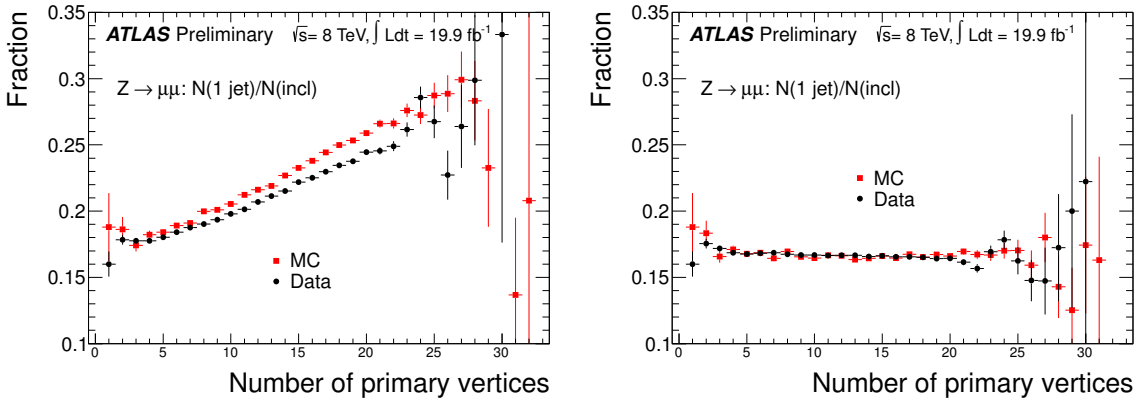

Figure 16: The ratio of $Z \to \mu\mu + 1$-jet events to all $Z \to \mu\mu$ candidates as a function of the number of reconstructed primary vertices in the event: No JVF requirement (left); with the $|\mathrm{JVF}| > 0.5$ requirement (right). Uncertainties are statistical.

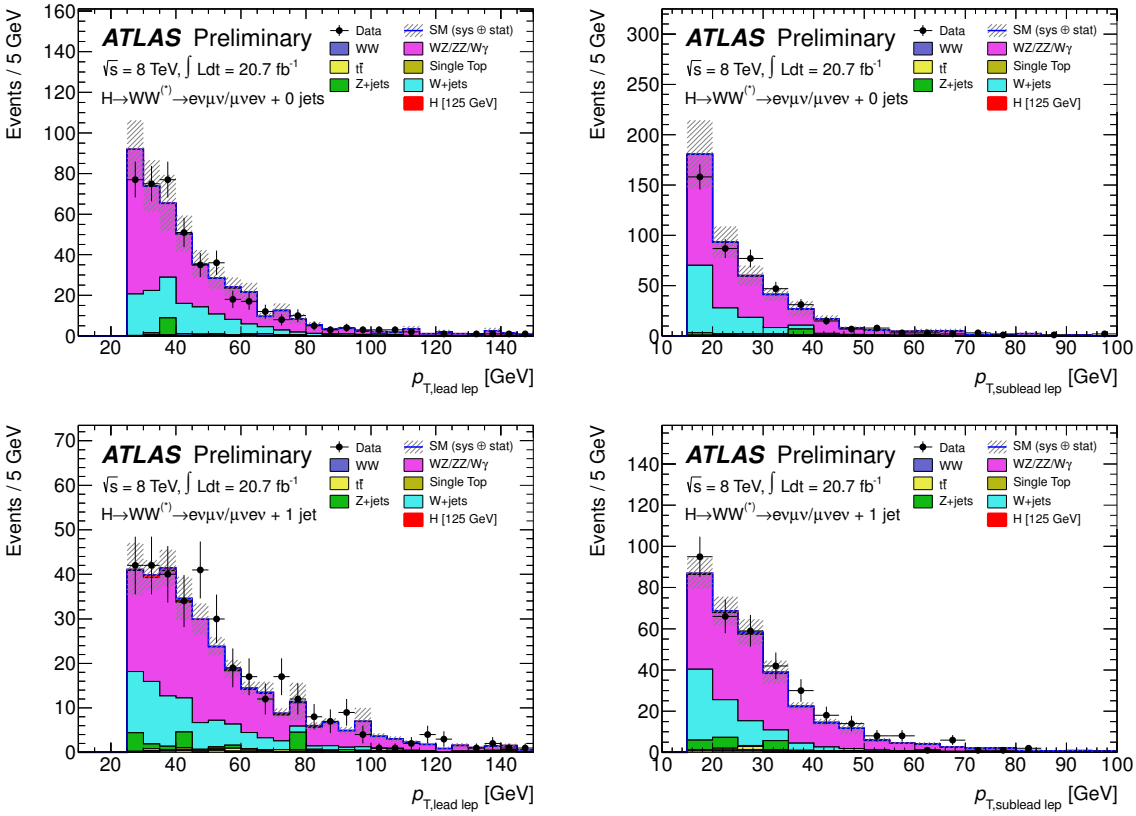

Figure 17: Distributions for the same-charge validation region: leading lepton p_{T} (top left) and subleading lepton p_{T} (top right) after the zero-jet $p_{\mathrm{T}}^{\ell\ell}$ cut and leading lepton p_{T} (bottom left) and subleading lepton p_{T} (bottom right) after the one-jet b-veto requirement. The $e\mu + \mu e$ channels are combined. The shaded area represents the uncertainty on the signal and background yields from statistical, experimental, and theoretical sources.

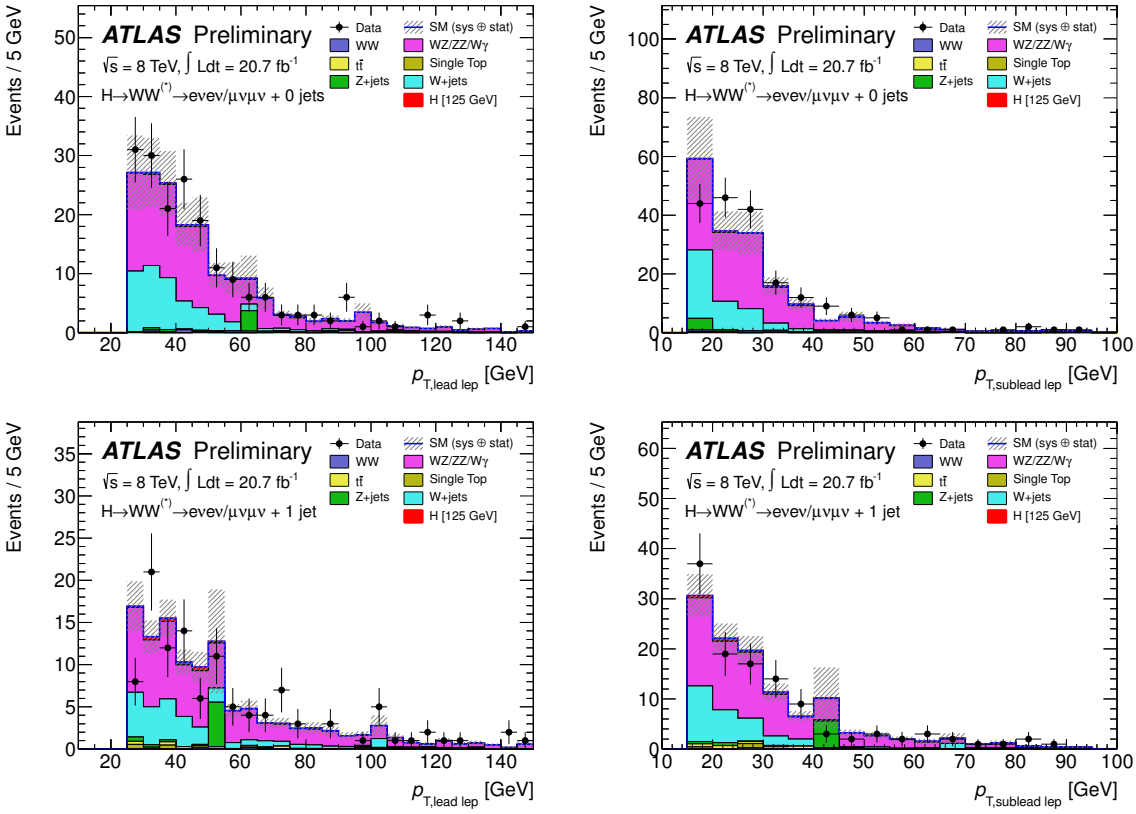

Figure 18: Distributions for the same-charge validation region: leading lepton p_{T} (top left) and subleading lepton p_{T} (top right) after the zero jet $p_{\mathrm{T}}^{\ell\ell}$ cut and leading lepton p_{T} (bottom left) and subleading lepton p_{T} (bottom right) after the one jet b-veto requirement. The ee and $\mu\mu$ channels are combined. The shaded area represents the uncertainty on the signal and background yields from statistical, experimental, and theoretical sources.

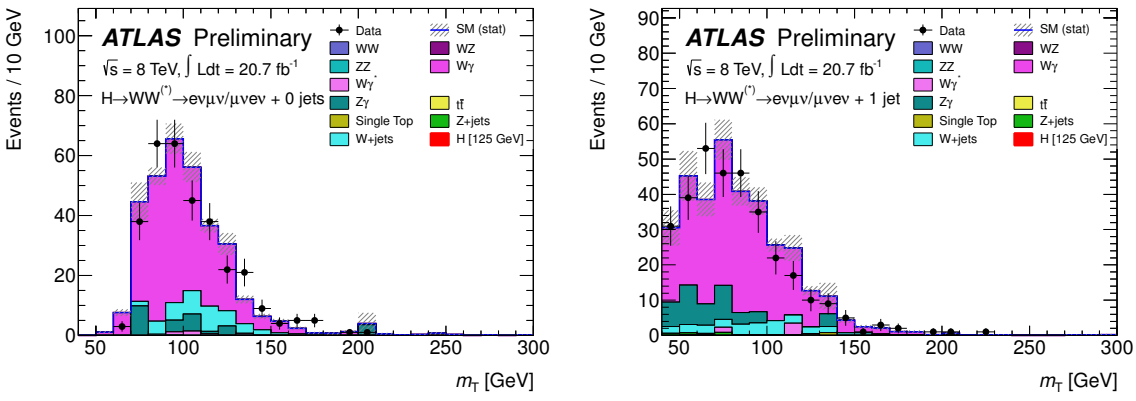

Figure 19: m_T distributions for the same-charge $W\gamma$ validation region: in the zero-jet (left) and one-jet (right) selection. The $e\mu$ and μe channels are combined. The shaded area represents the uncertainty on the signal and background yields from statistical, experimental, and theoretical sources.

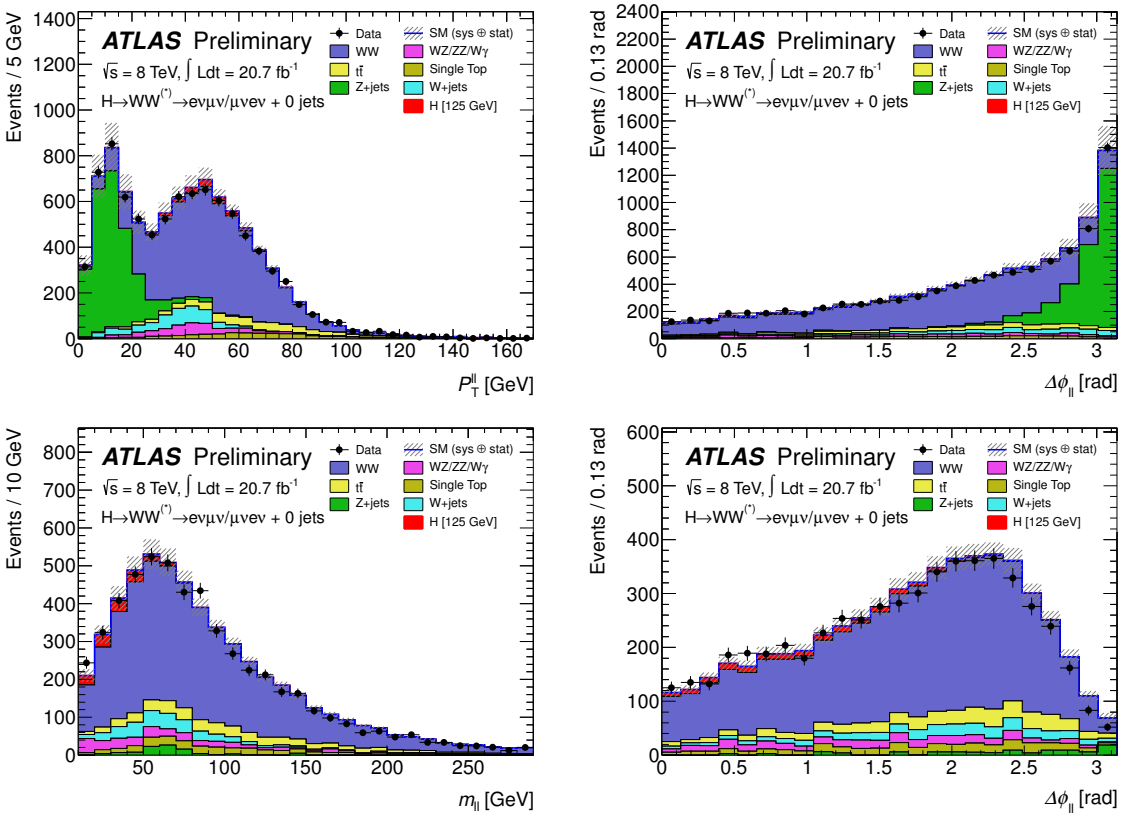

Figure 20: Kinematic distributions in the $N_{\text{jet}} = 0$ channel: $p_{\text{T}}^{\ell\ell}$ (top left) and $|\Delta\phi_{\ell\ell}|$ (top right) after the zero jet veto and $m_{\ell\ell}$ (bottom left) and $|\Delta\phi_{\ell\ell}|$ (bottom right) after the cut on $p_{\text{T}}^{\ell\ell}$. The signal is added on top of the background. The WW and top backgrounds are scaled to use the normalisation derived from the corresponding control regions described in the text. The shaded area represents the uncertainty on the signal and background yields from statistical, experimental, and theoretical sources.

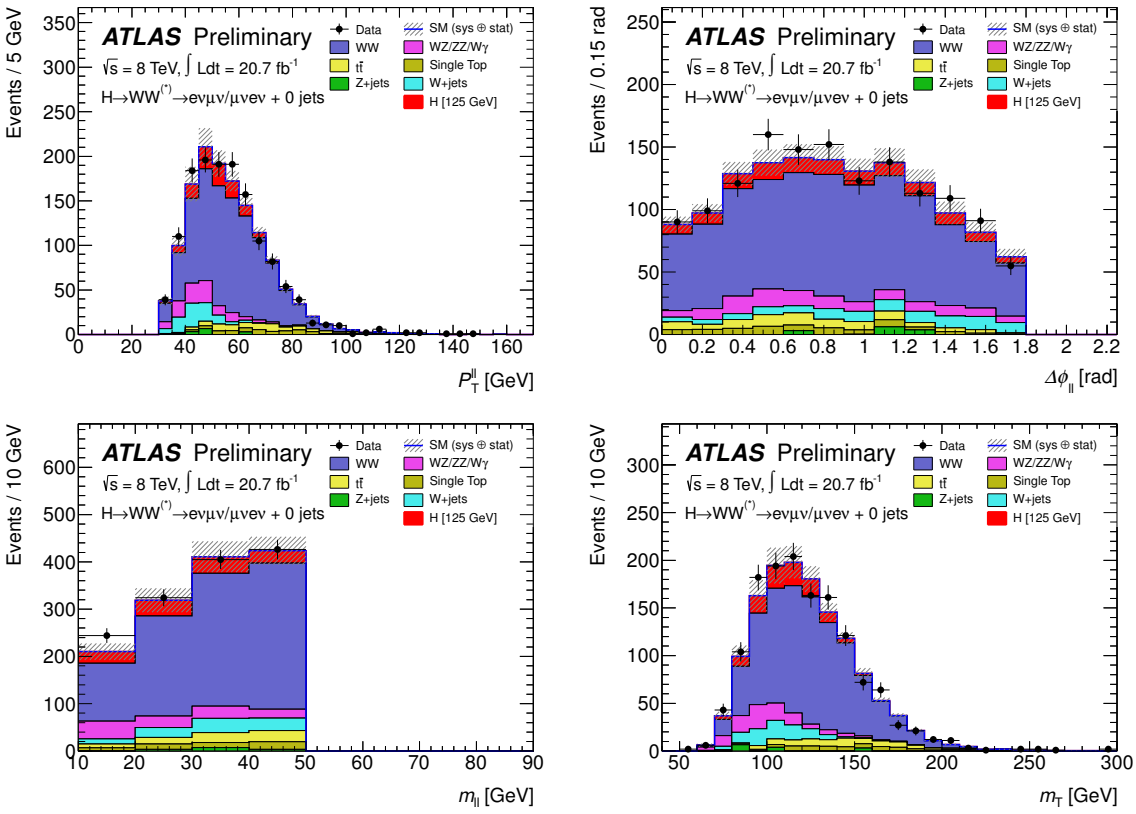

Figure 21: Kinematic distributions in the $N_{\text{jet}} = 0$ channel after the full selection: $p_{\text{T}}^{\ell\ell}$ (top left), $|\Delta\phi_{\ell\ell}|$ (top right), $m_{\ell\ell}$ (bottom left), and m_{T} (bottom right). The $e\mu$ and μe channels are combined. The signal is added on top of the background. The WW and top backgrounds are scaled to use the normalisation derived from the corresponding control regions described in the text. The shaded area represents the uncertainty on the signal and background yields from statistical, experimental, and theoretical sources.

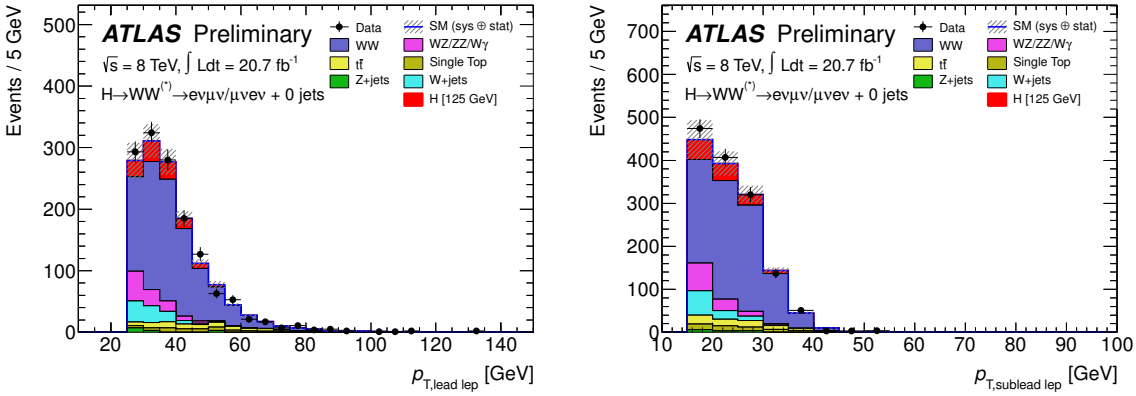

Figure 22: Kinematic distributions in the $N_{\text{jet}} = 0$ channel after the full selection: leading lepton p_{T} (left) and sub-leading lepton p_{T} (right). The $e\mu$ and μe channels are combined. The signal is added on top of the background. The WW and top backgrounds are scaled to use the normalisation derived from the corresponding control regions described in the text. The shaded area represents the uncertainty on the signal and background yields from statistical, experimental, and theoretical sources.

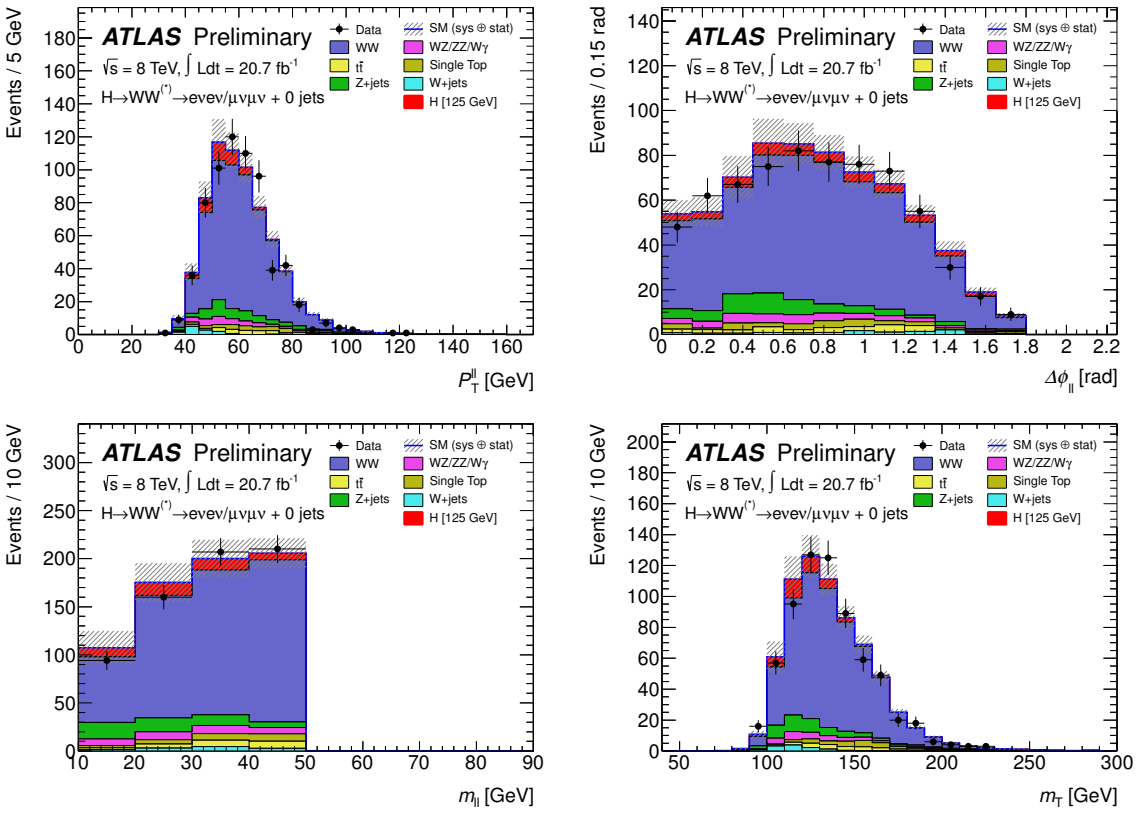

Figure 23: Kinematic distributions in the $N_{\text{jet}} = 0$ channel after the full selection: $p_{\text{T}}^{\ell\ell}$ (top left), $|\Delta\phi_{\ell\ell}|$ (top right), $m_{\ell\ell}$ (bottom left), and m_{T} (bottom right). The ee and $\mu\mu$ channels are combined. The signal is added on top of the background. The WW and top backgrounds are scaled to use the normalisation derived from the corresponding control regions described in the text. The shaded area represents the uncertainty on the signal and background yields from statistical, experimental, and theoretical sources.

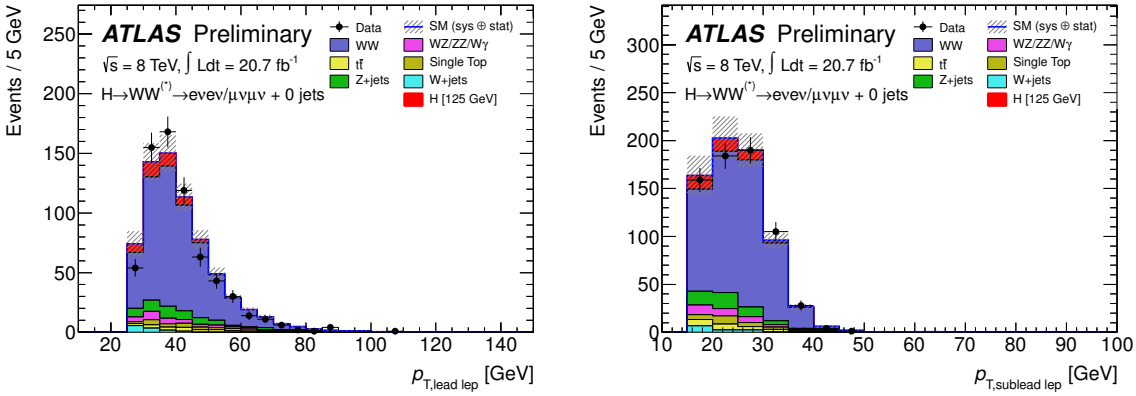

Figure 24: Kinematic distributions in the $N_{\text{jet}} = 0$ channel after the full selection: leading lepton p_{T} (left) and sub-leading lepton p_{T} (right). The ee and $\mu\mu$ channels are combined. The signal is added on top of the background. The WW and top backgrounds are scaled to use the normalisation derived from the corresponding control regions described in the text. The shaded area represents the uncertainty on the signal and background yields from statistical, experimental, and theoretical sources.

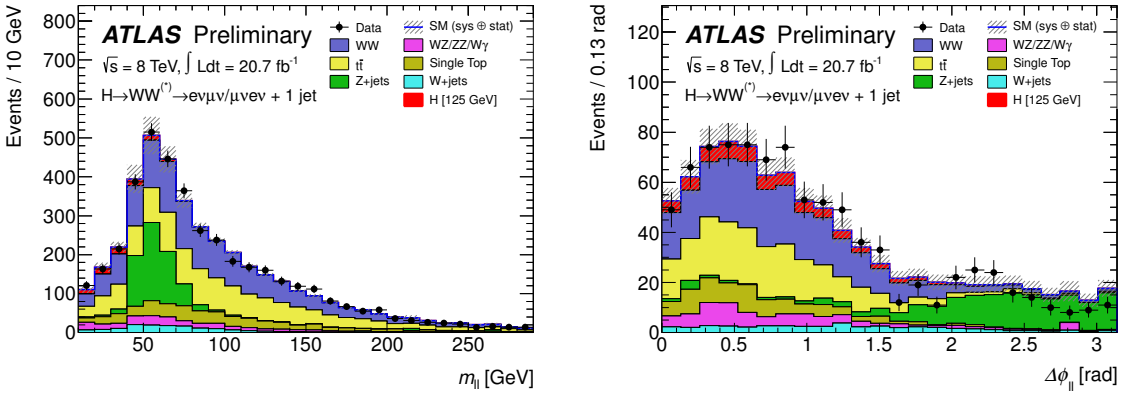

Figure 25: Kinematic distributions in the $N_{\text{jet}} = 1$ channel: $m_{\ell\ell}$ after the $Z \to \tau\tau$ veto (left) and $|\Delta\phi_{\ell\ell}|$ after the cut on $m_{\ell\ell}$ (right), The signal is added on top of the background. The WW and top backgrounds are scaled to use the normalisation derived from the corresponding control regions described in the text. The shaded area represents the uncertainty on the signal and background yields from statistical, experimental, and theoretical sources.

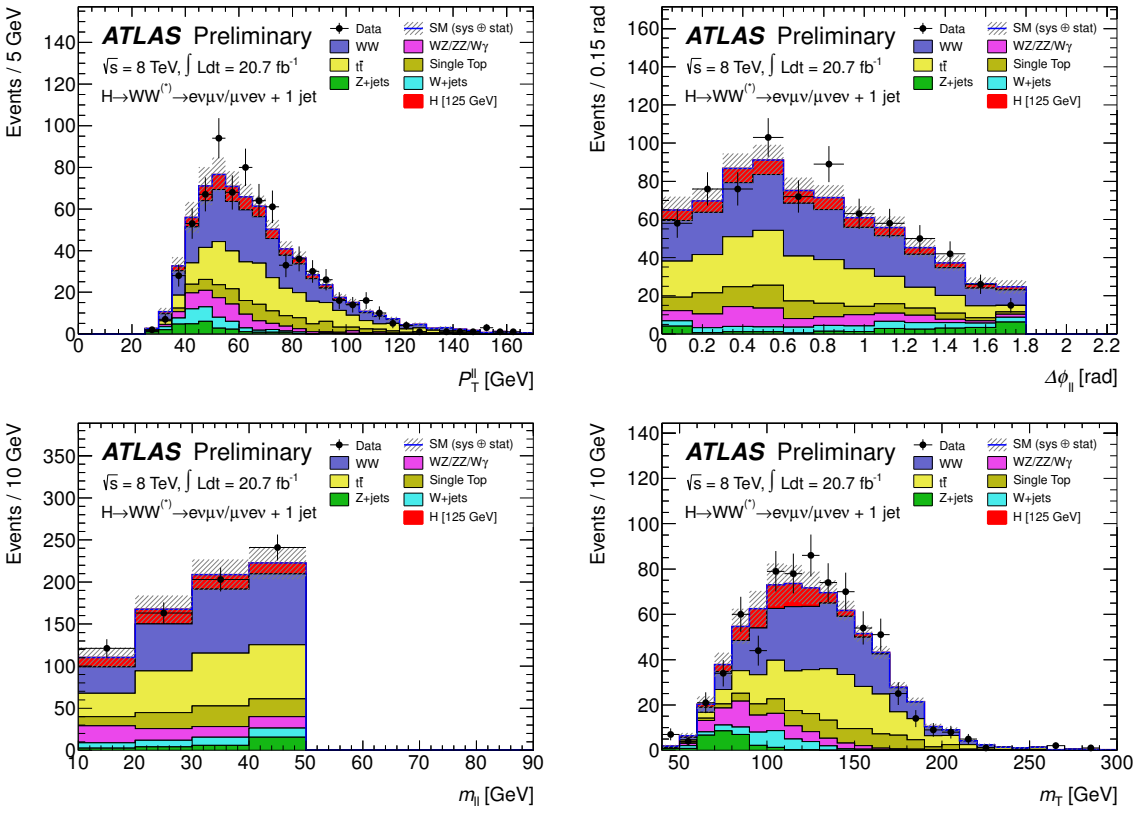

Figure 26: Kinematic distributions in the $N_{\text{jet}} = 1$ channel after the full selection: $p_{\text{T}}^{\ell\ell}$ (top left), $|\Delta\phi_{\ell\ell}|$ (top right), $m_{\ell\ell}$ (bottom left), and m_{T} (bottom right). The eμ and μe channels are combined. The signal is added on top of the background. The WW and top backgrounds are scaled to use the normalisation derived from the corresponding control regions described in the text. The shaded area represents the uncertainty on the signal and background yields from statistical, experimental, and theoretical sources.

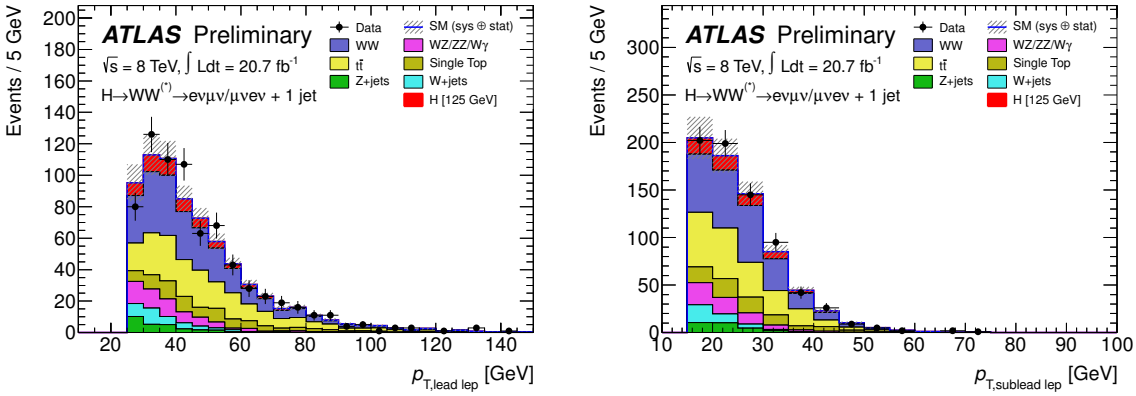

Figure 27: Kinematic distributions in the $N_{\text{jet}} = 1$ channel after the full selection: leading lepton p_{T} (left) and sub-leading lepton p_{T} (right). The $e\mu$ and μe channels are combined. The signal is added on top of the background. The WW and top backgrounds are scaled to use the normalisation derived from the corresponding control regions described in the text. The shaded area represents the uncertainty on the signal and background yields from statistical, experimental, and theoretical sources.

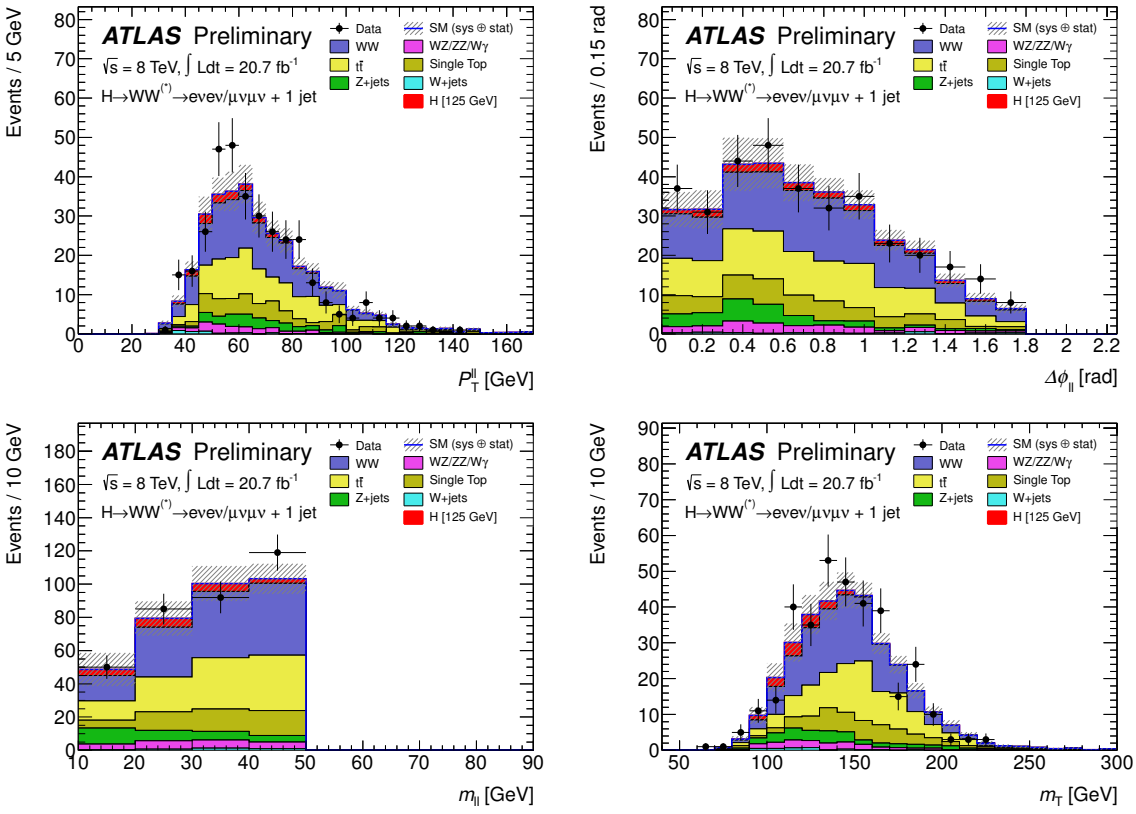

Figure 28: Kinematic distributions in the $N_{\text{jet}} = 1$ channel after the full selection: $p_{\text{T}}^{\ell\ell}$ (top left), $|\Delta\phi_{\ell\ell}|$ (top right), $m_{\ell\ell}$ (bottom left), and m_{T} (bottom right). The ee and $\mu\mu$ channels are combined. The signal is added on top of the background. The WW and top backgrounds are scaled to use the normalisation derived from the corresponding control regions described in the text. The shaded area represents the uncertainty on the signal and background yields from statistical, experimental, and theoretical sources.

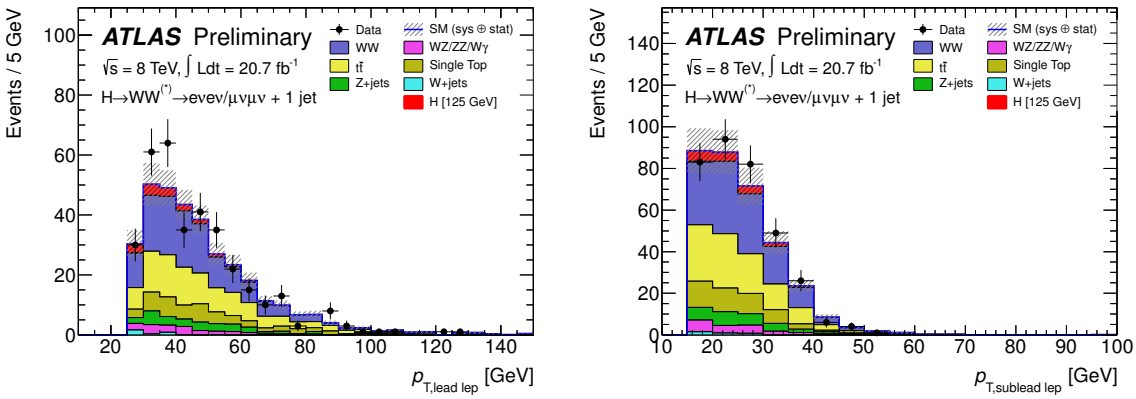

Figure 29: Kinematic distributions in the $N_{\text{jet}} = 1$ channel after the full selection: leading lepton p_{T} (left) and sub-leading lepton p_{T} (right). The ee and $\mu\mu$ channels are combined. The signal is added on top of the background. The WW and top backgrounds are scaled to use the normalisation derived from the corresponding control regions described in the text. The shaded area represents the uncertainty on the signal and background yields from statistical, experimental, and theoretical sources.

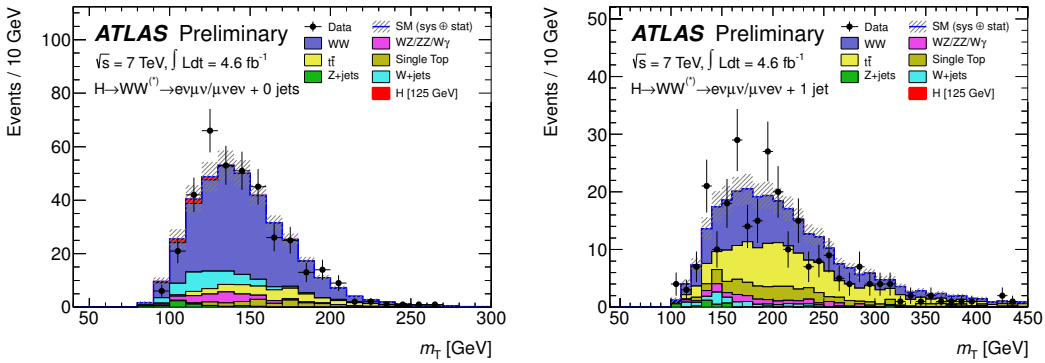

Figure 30: m_{T} distributions in the WW control region in the $N_{\mathrm{jet}} = 0$ (left) and $N_{\mathrm{jet}} = 1$ (right) analyses, before normalising the simulation to the rate in data. Only $e\mu + \mu e$ channels and $\sqrt{s} = 7$ TeV data are shown. The top backgrounds are scaled using the normalisation derived from the corresponding control regions described in the text. The shaded area represents the uncertainty on the signal and background yields from statistical, experimental, and theoretical sources.

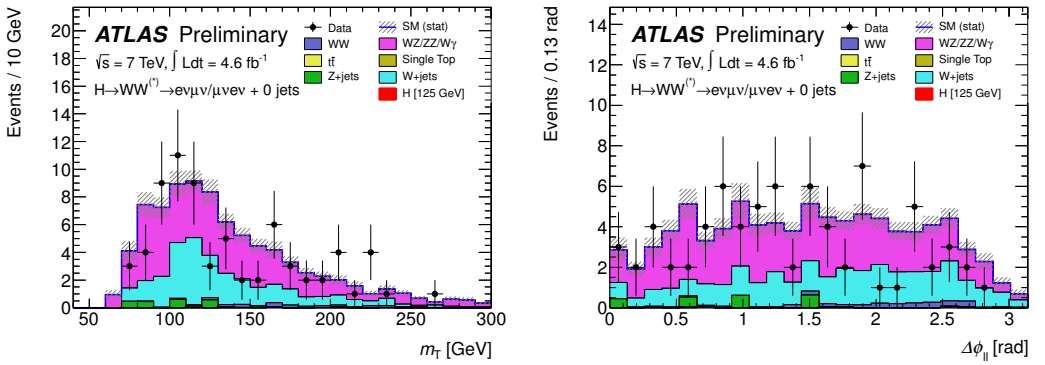

Figure 31: Distribution of m_{T} (left) and $\Delta\phi_{\ell\ell}$ (right) in the same-charge validation region in the $N_{\mathrm{jet}} = 0$ sample after the $p_{\mathrm{T}}^{\ell\ell}$ requirements. Only $e\mu + \mu e$ channels and $\sqrt{s} = 7$ TeV data are shown. The shaded area represents the uncertainty on the signal and background yields from statistical, experimental, and theoretical sources.

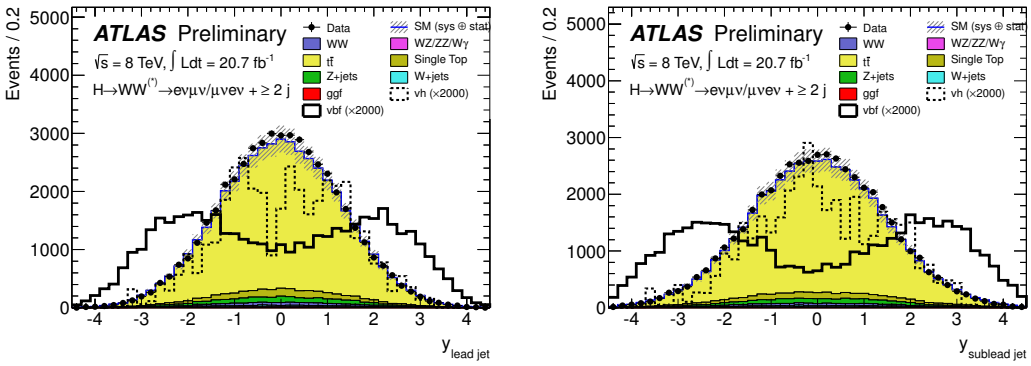

Figure 32: Rapidity distributions of the leading and sub-leading tagging jets. The distribution is shown at the 2 jets requirement, the signal is magnified by a factor 2000 to show the peculiar forward distribution of jets from the VBF process. The shaded area represents the uncertainty on the signal and background yields from statistical, experimental, and theoretical sources.

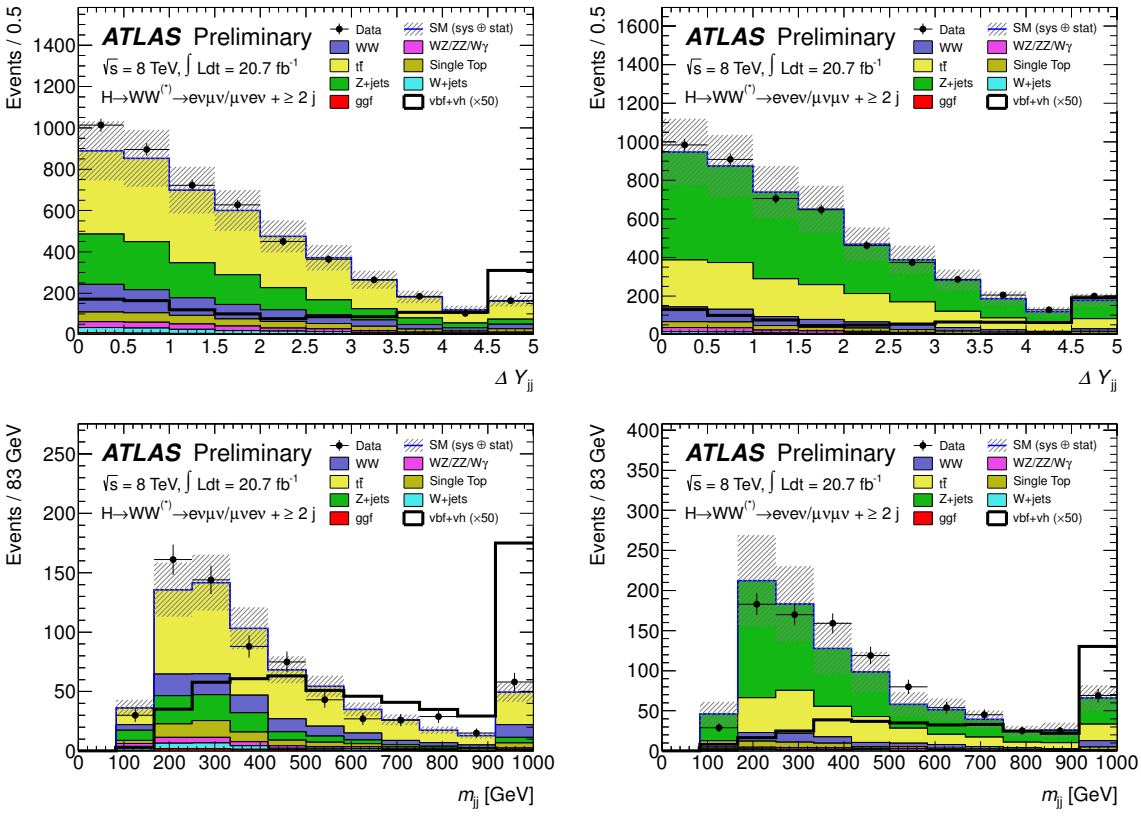

Figure 33: The $|\Delta y_{jj}|$ and m_{jj} distributions after the $p_{\mathrm{T}}^{\mathrm{tot}} < 45$ GeV cut. $p_{\mathrm{T}}^{\mathrm{tot}}$ is defined as the total transverse momentum of all leptons, jets and missing E_T passing the selection. The m_{jj} distribution is shown after the $|\Delta y_{jj}| > 2.8$ cut. The shaded area represents the uncertainty on the signal and background yields from statistical, experimental, and theoretical sources.

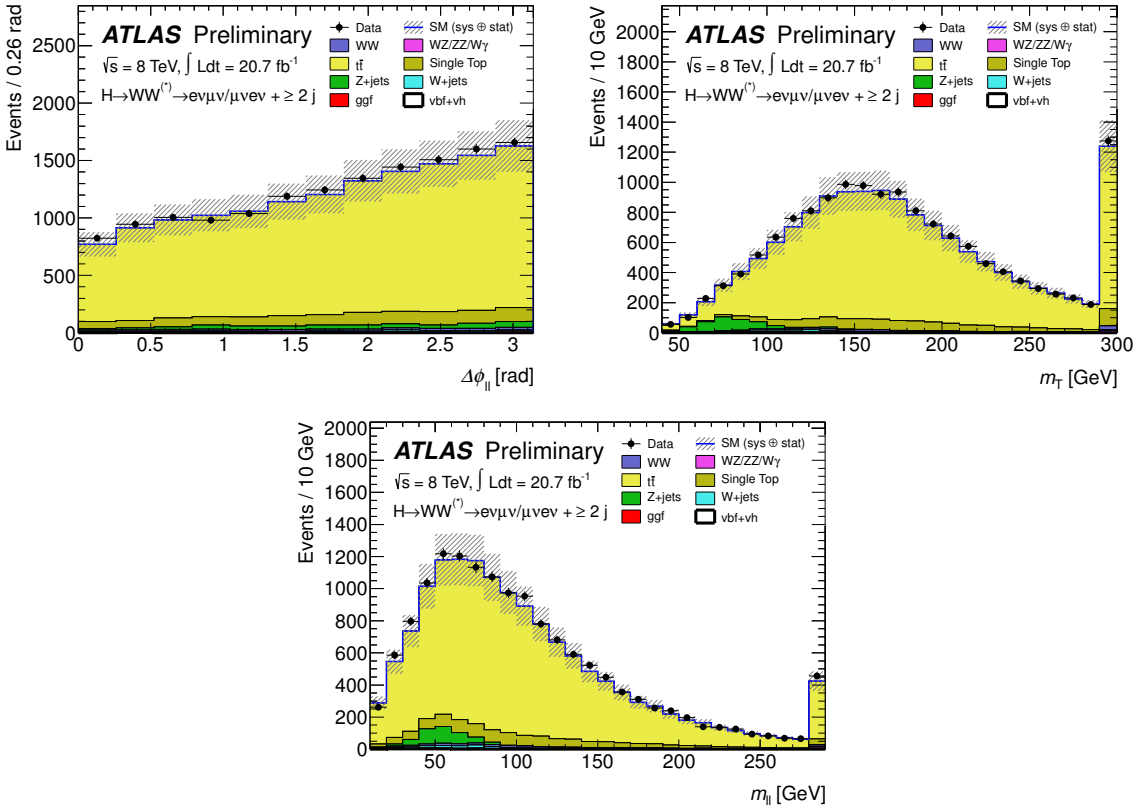

Figure 34: The $|\Delta\phi_{\ell\ell}|$, m_{T} and $m_{\ell\ell}$ distributions after the $p_{\mathrm{T}}^{\mathrm{tot}} < 45$ GeV cut in the top CR, defined by the requirement of one and only one b tagged jet . $p_{\mathrm{T}}^{\mathrm{tot}}$ is defined as the total transverse momentum of all leptons, jets and missing E_T passing the selection. The shaded area represents the uncertainty on the signal and background yields from statistical, experimental, and theoretical sources.

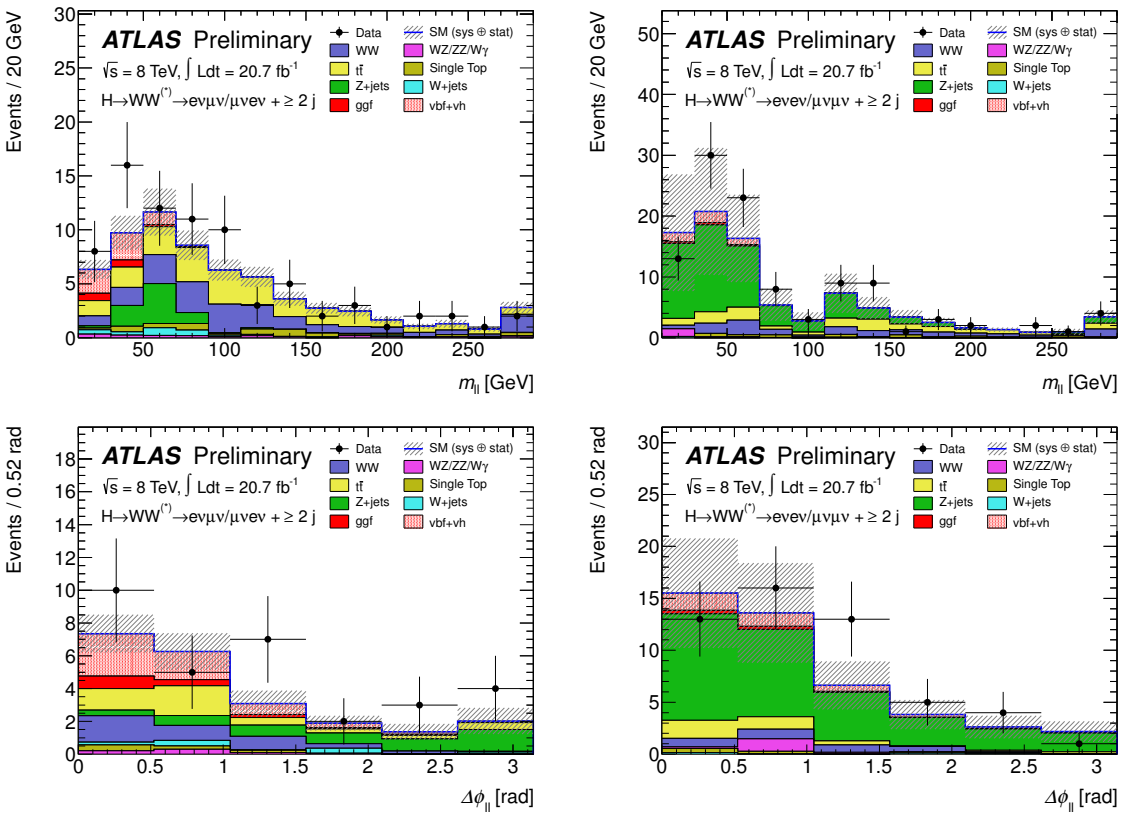

Figure 35: The $m_{\ell\ell}$ and the $|\Delta\phi_{\ell\ell}|$ distributions after the outside lepton veto cut, accepting events with leptons between the two tagging jets. $|\Delta\phi_{\ell\ell}|$ is shown after the $m_{\ell\ell} < 60$ GeV cut. The shaded area represents the uncertainty on the signal and background yields from statistical, experimental, and theoretical sources.